

Roadmap for the Development of Transition Metal Oxide Cathodes for Rechargeable Zinc-Ion Batteries

Caio Miranda Miliante,* Storm Gourley, Brian D. Adams, Drew Higgins, and Oleg Rubel



Cite This: *J. Phys. Chem. C* 2024, 128, 17261–17273



Read Online

ACCESS |



Metrics & More

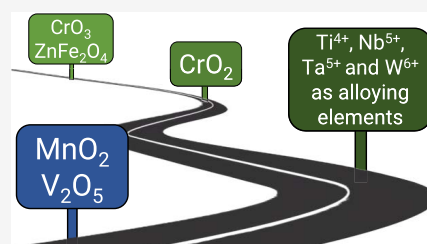


Article Recommendations



Supporting Information

ABSTRACT: Rechargeable zinc-ion batteries (RZIBs) are a promising multivalent battery technology for grid-scale energy storage applications, thanks to their abundant materials, lower environmental impact, and higher safety due to the use of aqueous electrolytes as compared to lithium-based batteries. However, there is still a lack of cathode materials with suitable stability and performance for reliable implementation in these energy storage applications. In this study, we utilized readily available thermodynamic properties obtained from first-principle atomistic simulations to calculate the intercalation potential of zinc in numerous potential candidate cathode materials. We confined our chemical space to simple transition metal oxides (M_xO_y , where M is a transition metal). While some materials in this class were previously experimentally studied (e.g., MnO_2 , V_2O_5 , and MoO_3), a literature survey revealed multiple oxides for which no prior investigation on their use as cathodes for RZIBs had been performed. We considered previously reported structures with similar atomic arrangements for the charged and discharged phases, the feasibility of experimental realization of the materials, the electrochemical stability of the charged cathode in an aqueous environment, and the potential degradation of aqueous electrolytes in our analysis. We mapped the zinc intercalation potential for over 50 redox pairs involving oxides of 12 different elements. These calculated theoretical potentials were then compared to previously obtained experimental results, with a relatively small difference between them (mean absolute error of 0.11 V), demonstrating the predictive capabilities of the utilized methodology. The failure mechanism for the experimentally observed capacity fade was determined from the electrochemical stability analysis to be related to the dissolution of the transition metal during battery cycling. Fully stable transition metals in the RZIB potential and pH operating conditions were discovered and proposed for use as alloying elements in RZIB cathodes to improve the capacity retention. Previously overlooked materials with high intercalation potential (above 1.6 V vs Zn/Zn^{2+}) were then proposed as cathode materials for RZIBs. The Zn^{2+} intercalation potential mapping and electrochemical stability analysis for the oxide redox pairs achieved in this study provide a roadmap for future experimental investigations of novel cathode materials for RZIBs.



INTRODUCTION

A crucial shift in energy resources from fossil fuels to renewable power generation is currently ongoing to support efforts to achieve a sustainable future. However, due to the inherent variable character of wind and solar energy, a simple and direct integration into modern electricity grids is not technologically viable.^{1,2} To address this limitation, considerable focus is currently being given to the research and implementation of grid-scale energy storage solutions capable of bridging the natural time gap between energy conversion and utilization.^{1–4}

Rechargeable battery systems have become the preeminent technology in new grid-scale energy storage installations due to their modularity and independence from existing geographical features since the presence of elevation changes and bodies of water are not as crucial as it is for pumped hydro.^{4–7} Another positive aspect of the integration of batteries at the grid-scale level is their flexible discharge time scales, which can range from seconds for preventing line faults and controlling voltage up to tens of hours, which is important for ensuring reliable delivery of energy to meet the demand of the grid.^{1,5,8} Battery

technologies that can operate reliably with discharge cycles lasting more than 2 h are of major research interest, as continuous operation in this time scale is considered crucial for current and future grid-scale stationary energy storage deployments.⁸ While lithium-ion batteries (LIBs) comprise the majority of the newly gained capacity for grid-scale energy balancing, the scarcity of raw materials for these systems has motivated researchers to focus on batteries with more abundant working ions, such as Ca^{2+} , Mg^{2+} , and Al^{3+} .^{6,9–12}

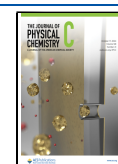
Rechargeable zinc-ion batteries (RZIBs) are one of these new technologies and offer several benefits in terms of balancing performance, cost, environmental impact, and material abundance.¹³ Continuous Zn stripping/plating from

Received: May 23, 2024

Revised: September 17, 2024

Accepted: September 24, 2024

Published: October 7, 2024



metallic Zn anodes in aqueous media allows for the use of water-based electrolytes (rechargeable aqueous zinc-ion batteries (RAZIBs)).^{14–16} Due to the use of aqueous electrolytes, RAZIBs are considered a safer option, as there are concerns over the flammability and toxicity of nonaqueous electrolytes.^{10,17–19} However, the risk of degradation of the aqueous electrolyte (i.e., the hydrogen evolution reaction (HER) and the oxygen evolution reaction (OER)) forces the RAZIB to have a narrower operating voltage window,^{20,21} which impedes achieving batteries with higher energy densities due to the upper limit for Zn^{2+} intercalation potential. The possibility of water splitting and the electrochemical stability of the cathode during the intercalation–deintercalation cycles are currently the two major bottlenecks to the progress and commercial realization of RAZIBs.²²

Simple transition metal oxides (M_xO_y , where M is a transition metal) have previously been experimentally investigated as cathode materials for RAZIBs,^{10,23} with manganese (e.g., Mn_2O_3 , MnO_2) and vanadium (e.g., V_2O_3 , VO_2 , V_2O_5)-based oxides being the most prominent ones.^{10,22,24–32} Oxides of manganese were initially attractive due to their abundance, ease of processing, and eco-friendly nature, with their considerably high intercalation potential (ca. 1.5 V vs Zn/Zn^{2+}) supporting their continuous research interest.^{22,23,33} Furthermore, multiple previous reports have even claimed the development of highly stable MnO_2 cathodes for RAZIBs, with capacity retention greater than 90% after more than 1000 cycles.^{34–37} However, these high stability results are only achievable when cycling at high current densities (greater than 1 A g^{-1}), consequently having battery cycles lasting only minutes instead of several hours as it is necessary for their realistic operation in grid-scale energy storage.⁸ When cycling a RAZIB with Mn oxide cathodes at lower current densities (therefore, longer lasting cycles), a considerable capacity fade has been shown to occur over time.^{24,38,39} The dissolution of Mn^{2+} into the electrolyte and codeposition of nonstoichiometric manganese oxides is considered as the reason behind the capacity loss, with it currently being the main concern over the use of Mn oxide cathodes in RAZIBs.^{10,22,24,25,40}

Vanadium oxide cathodes are known for having a higher specific capacity than their Mn counterparts; however, they display a lower Zn^{2+} intercalation potential (ca. 1.0 V vs Zn/Zn^{2+}).^{10,41–43} Unfortunately, considerable capacity fade is still present at practical charge rates, with structural collapse, side product formation, and dissolution of the active material in the aqueous media being attributed to the capacity loss.^{41,44} Other simple transition metal oxides, such as TiO_2 , Fe_3O_4 , Fe_2O_3 , Co_3O_4 , Cu_2O , CuO , MoO_2 , MoO_3 , and WO_3 have also been experimentally investigated as cathodes for RAZIBs; however, their high capacity fade, low specific capacity, and/or associated low intercalation potential can be considered as some of the reasons for the overall lower research interest when compared to Mn- and V-based materials.^{45–54}

Exploration and screening of suitable cathode materials for rechargeable battery systems can also be expedited by providing theoretical estimates of the thermodynamic properties associated with the charged and discharged phases. This approach has been regularly used for capturing the associated potential for Li^+ intercalation in LIBs,^{55,56} having also since been used for modeling multivalent ion batteries.^{57,58} Up to now, there have been limited computational efforts to calculate the intercalation potential for RZIB cathode materials. Le et al.⁵⁹ reported calculations of the Zn^{2+} deintercalation potential

in $\alpha\text{-MnO}_2$, showing that hydration, along with the Hubbard U correction in density functional theory (DFT), are important factors for reproducing the experimental intercalation potential. Our group showed that it is possible to reproduce the experimental deintercalation potential in electrolytic MnO_2 at the Perdew–Burke–Ernzerhof (PBE)⁶⁰ + U level of theory using the spinel ($\lambda\text{-Zn}_{0-1}\text{Mn}_2\text{O}_4$) structure as a model without hydration.⁴⁰ A similar approach, also at the PBE + U level, was pursued for the investigation of vanadium oxides. Gautam et al.³¹ studied both the α and δ polymorphs of V_2O_5 , calculating potentials of 0.68 and 1.09 V vs Zn/Zn^{2+} for the respective phases. Zhu et al.³² observed experimentally a combined intercalation of H^+ and Zn^{2+} into the VO_2 host structure, with DFT calculations of sequential intercalation of these ions reproducing their experimental results.

Figure 1 summarizes the current investigation efforts on both the experimental and theoretical sides regarding the

Exp. Ti	V	Cr	Mn	Fe	Co	Ni	Cu
Theo. Zr	Nb	Mo	Tc	Ru	Rh	Pd	Ag
Hf	Ta	W	Re	Os	Ir	Pt	Au

Figure 1. Periodic table representation relating the transition metal elements and the existence of previous investigations over the use of their simple oxides as cathodes for RZIBs. The blue coloring indicates simple oxides that have the Zn^{2+} intercalation potential previously reported experimentally (shaded upper left corner) and theoretically (shaded bottom right corner) in the literature for at least one of their redox states, with the white background indicating no previous report. The elements that are crossed out were not considered in this study, with the explanation for this decision given in the Computational Methods section.

utilization of simple transition metal oxides as cathodes in RZIBs. While 8 out of the 12 elements considered in this study have had at least one of their oxides experimentally studied as a cathode for RZIBs, only two of them (V- and Mn-oxides) have had the Zn^{2+} intercalation potential theoretically investigated. As elements can be found in different oxidation states, multiple simple oxides can be obtained for each transition metal (e.g., MO , M_2O_3 , and MO_3). When considering each simple oxide for which the transition metals contemplated here can be found (TiO , Ti_2O_3 , TiO_2 , Ti_3O_5 for Ti, for example),⁶¹ a literature survey shows that close to only 40% of them have been previously experimentally investigated for their use as cathodes for RZIBs and only 10% theoretically. Therefore, even though transition metal oxides have been on the vanguard of studied cathodes for RZIBs, there are still a considerable amount of unexplored materials that could come to be of scientific interest.

When surveying the literature for approaches to investigate and compare the intercalation potential of cathodes from different materials, the utilization of Goodenough diagrams in the study of cathode materials for LIBs was identified.^{62,63} In these representations, the cathode materials' redox pair energy versus Li^+/Li^0 is displayed graphically, allowing for a direct comparison of the intercalation potential for different materials.^{62,64} However, the RZIB literature still lacks a similar systematic investigation of the intercalation potential for

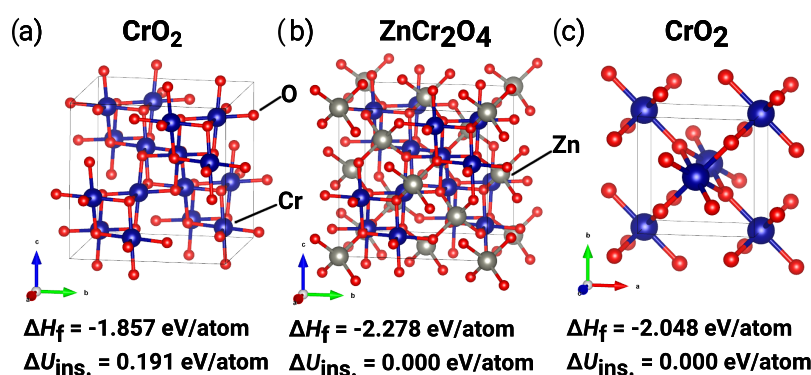


Figure 2. Crystal structure and thermodynamic properties of selected Cr oxides. (a) CrO₂ (mp-1400837) and (b) ZnCr₂O₄ (mp-19410) structures were identified by the Battery Explorer tool as suitable charged and discharged phases for Zn²⁺ (de)intercalation. (c) The thermodynamically most stable phase of CrO₂ (mp-19177), for which a similarly arranged ZnCr₂O₄ structure is unavailable.

different cathodes, which could expedite the discovery of novel cathode materials and ultimately contribute to the realization of commercial RZIBs.

In this paper, we used DFT-calculated thermodynamic properties available within the Materials Project database⁶⁵ to predict the reversible Zn²⁺ intercalation potential in various simple transition metal oxides for their application as cathodes in RZIBs. The Battery Explorer application⁶⁵ and the Phase Diagram analysis tool^{65,66} were used to identify atomic structures of suitable candidate materials for Zn²⁺ intercalation and their associated formation enthalpy. This methodology was employed for screening the Zn²⁺ intercalation potential of more than 50 oxide redox pairs from 12 different transition metals. The predicted Zn²⁺ intercalation potentials were then compared to previously published experimental and theoretical results for transition metal oxides working as cathodes in RZIBs in order to validate the results presented here. The possible utilization of these materials in aqueous systems was also evaluated by (i) comparing the Zn²⁺ intercalation potential with the boundaries of electrolyte stability (OER and HER), as well as (ii) evaluating the electrochemical stability of the studied oxides within the relevant pH and potential ranges by using experimentally obtained Pourbaix diagrams. To support the analysis of the oxides' electrochemical stability obtained from the Pourbaix diagrams, the performance of MnO₂ as a cathode in aqueous media was experimentally pursued at different current densities. The failure mechanism of the MnO₂ cathode was identified by combining the results from the electrochemical stability analysis and the experimental tests. Based on these findings, other transition metal oxides that would fail similarly as cathode materials during operation were also identified. Transition metals that were found to be fully stable within the potential and pH window for RAZIB operation were then proposed as alloying elements to enhance the stability of cathode materials. Lastly, previously overlooked oxides with a high Zn²⁺ intercalation potential were suggested as potential cathode materials for RZIBs.

METHODOLOGY

Computational Methods. Simple transition metal oxides (M_xO_y, where M is a transition metal) were selected to explore their theoretical potential as cathodes for RZIBs. After considering aspects such as commercial availability, toxicity, price, and the existence and quantity of structures reported in the Materials Project database,⁶⁵ the following elements' oxides

were chosen for the survey: Ti, V, Cr, Mn, Fe, Co, Ni, Cu, Nb, Mo, Ta, and W. Before the theoretical potential of transition metal oxides is modeled, it is first necessary to establish the operating mechanism that these materials undergo when used as cathodes for RZIBs. Several mechanisms have been previously proposed in the literature for the operation of RZIB cathodes, including Zn²⁺ intercalation, conversion reactions, active material dissolution/redeposition, and H⁺ and Zn²⁺ coininsertion.^{67,68} For example, in the case of MnO₂ cathode materials, all of these mechanisms have been reported to occur during battery cycling, with no consensus currently found on the operating mechanism for this oxide.^{13,22,67,68} However, when examining the operating principle reported experimentally for other transition metal oxides (e.g., V₂O₅, VO₂, MoO₃) as cathodes for RZIBs, an agreement toward a Zn²⁺ insertion mechanism is observed.^{13,30,51,67,69} For this reason, Zn²⁺ intercalation was considered here as the operating mechanism when calculating the cathode materials' theoretical potential. By doing so, better agreement with the working potential of previously studied materials, as well as a more accurate prediction of the potential for unexplored transition metal oxides, is expected.

To model the Zn²⁺ intercalation potential of the transition metal oxides, the Battery Explorer suite⁶⁵ was used to identify the possible redox pairs of charged (M_xO_y) and discharged (Zn_zM_xO_y) structures that could be obtained for each metal site M, taking into account similarities in the atomic arrangement of both phases that would allow for a reversible Zn²⁺ (de)intercalation. A representation of such similarity is illustrated in Figure 2, where the atomic structure of the considered charged CrO₂ (Figure 2a) and discharged ZnCr₂O₄ (Figure 2b) phases for the Cr⁴⁺/Cr³⁺ redox pair can be seen. The thermodynamic properties are listed alongside each structure, where ΔH_f is its formation enthalpy and $\Delta U_{ins.}$ is its energy above the convex hull. Both quantities are later used for the calculation of the Zn²⁺ intercalation energy. While for Cr⁴⁺/Cr³⁺, redox pair structures with similar atomic arrangements were available; this was not the case for every redox pair evaluated. In these situations, representative structures for both the charged and discharged phases were individually selected from the database for performing the calculations regardless of their atomic structure.

To evaluate the theoretical Zn²⁺ intercalation potential unique for each redox pair, we considered the formation energy of compounds at the convex hull

$$\Delta H_f^{\text{ch}}(M_xO_y) = \Delta H_f(M_xO_y) - \Delta U_{\text{ins.}}(M_xO_y) \quad (1)$$

by subtracting the energy above the hull ($\Delta U_{\text{ins.}}$, which represents a magnitude of instability) from the calculated formation enthalpy (ΔH_f). The convex hull (dashed line in Figure 3) is the line formed by linking the enthalpy of

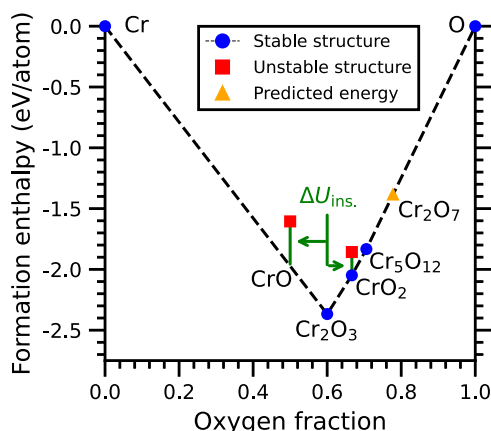


Figure 3. Convex hull diagram for the Cr–O system depicting the oxide structures that are considered thermodynamically stable (blue circles) and unstable (red squares), as well as the predicted energy for an oxide without a reported structure (orange triangle). The thermodynamic data for this diagram was obtained from Materials Project.⁶⁵

formation for the different reported structures throughout the composition spectra, given that no data point will have a lower enthalpy than the convex hull for the same composition. As a result, the formation enthalpy on the convex hull (ΔH_f^{ch}) denotes the lowest energy predicted for a certain phase. Therefore, by utilizing ΔH_f^{ch} for the calculation, a more accurate prediction of the Zn^{2+} intercalation potential is expected, as the structures that can be experimentally realized are anticipated to have lower formation enthalpy values obtained from DFT. An example of a convex hull diagram is presented in Figure 3 for the Cr–O system. Not necessarily for every oxide composition will there be a representative structure on the convex hull, as can be seen for CrO in Figure 3. Similarly, for other compositions, a representative structure may not even be available, as is the case for Cr_2O_7 . For the calculations performed in this study, if a considered phase (e.g., CrO_2) had a reported structure on the Materials Project database (e.g., mp-1400837 for CrO_2), its ΔH_f^{ch} was calculated using eq 1. However, if no structure for a desired oxide was available in the database, the predicted value for ΔH_f^{ch} was obtained directly from the convex hull diagram using the Phase Diagram analysis tool.^{65,66}

It should be noted that the crystal structure of the oxides is only considered here by the Battery Explorer tool,⁶⁵ which surveys the M_xO_y and $\text{Zn}_z\text{M}_x\text{O}_y$ structures with similar atomic arrangements that would allow for reversible Zn^{2+} (de)-intercalation. For the calculation of the Zn^{2+} intercalation potential, the oxide's formation enthalpy at the convex hull ΔH_f^{ch} is the only property related to the compound that is used. And as the numerical value for $\Delta H_f^{\text{ch}}(M_xO_y)$ is independent of the crystal structure of M_xO_y being considered for calculation, a single theoretical Zn^{2+} intercalation potential is assigned to each evaluated redox pair. This interdependency of the crystal structure on the calculation of the Zn^{2+} intercalation

potential can be seen for the $\text{Cr}^{4+}/\text{Cr}^{3+}$ redox pair. Both the CrO_2 structure considered feasible for intercalation (structure shown in Figure 2a, red square in Figure 3) and the CrO_2 structure at the convex hull (structure shown in Figure 2c, blue circle in Figure 3) will report the same ΔH_f^{ch} , and, consequently, the same Zn^{2+} intercalation potential will be assigned to them. While this methodology does not allow for the investigation of the impact of the oxide's crystal structure on its Zn^{2+} intercalation potential, better agreement with experimental results is expected by only considering the formation enthalpy at the convex hull for the calculation of Zn^{2+} intercalation potential. This expected higher accuracy is because materials that can be experimentally realized are predicted by DFT calculations to have a lower formation enthalpy. Also, previous theoretical investigations have shown significant underprediction of the Zn^{2+} intercalation potential depending on the crystal structure due to the calculated formation enthalpy of the discharged phase ($\text{Zn}_z\text{M}_x\text{O}_y$) being considerably greater than the value at the convex hull.⁴⁰ For this reason, a higher accuracy for the calculated Zn^{2+} intercalation potential is expected by considering only the formation enthalpies at the convex hull.

For a material to be viable as a cathode, it is first necessary for the Zn insertion to be energetically favorable. This can be assessed through the intercalation energy ΔH_{Zn} (in eV per Zn atom)

$$\Delta H_{\text{Zn}} = \frac{\Delta H_f^{\text{ch}}(\text{Zn}_z\text{M}_x\text{O}_y)(x + y + z) - \Delta H_f^{\text{ch}}(M_xO_y)(x + y)}{z} \quad (2)$$

Negative values of ΔH_{Zn} indicate favorable Zn insertion. The Zn^{2+} deintercalation potential of a $\text{Zn}_x\text{M}_y\text{O}_z$ compound is then obtained from the Nernst equation

$$E_{\text{Zn}} \approx -\frac{\Delta H_{\text{Zn}}}{n_e e} \quad (3)$$

where n_e is the number of electrons transferred per ion (2 for Zn^{2+}) and e is the elementary charge. Equation 3 is equivalent to that originally proposed by Aydinol et al.⁵⁶ Here, we neglect finite temperature effects, assuming that they largely cancel out, thus having the approximate sign.

For the development of this study, the DFT-calculated thermodynamic data available on the Materials Project database (v2022.10.28) were used,⁶⁵ with a generalized gradient approximation (GGA) parametrization for the exchange–correlation functional. To achieve better agreement between the different chemical systems studied, the results reported in the database already account for anion correction and GGA/GGA + U mixing schemes.^{70,71} The anion correction (for O in this case) aims to account for the errors in the calculated formation energy raised from the change in electron localization when these elements are at their standard states and with a negative oxidation state in the solid structure.⁷⁰ An additional Hubbard U correction to GGA was implemented for the transition metal sites in oxide systems as it has been shown to help more accurately capture their chemical properties. In this case, it is applied to V, Cr, Mn, Fe, Co, Ni, Mo, and W sites.⁷¹ For the other systems, results from standard GGA calculations were reported by the database, with a mixing scheme applied to consider both GGA and GGA + U

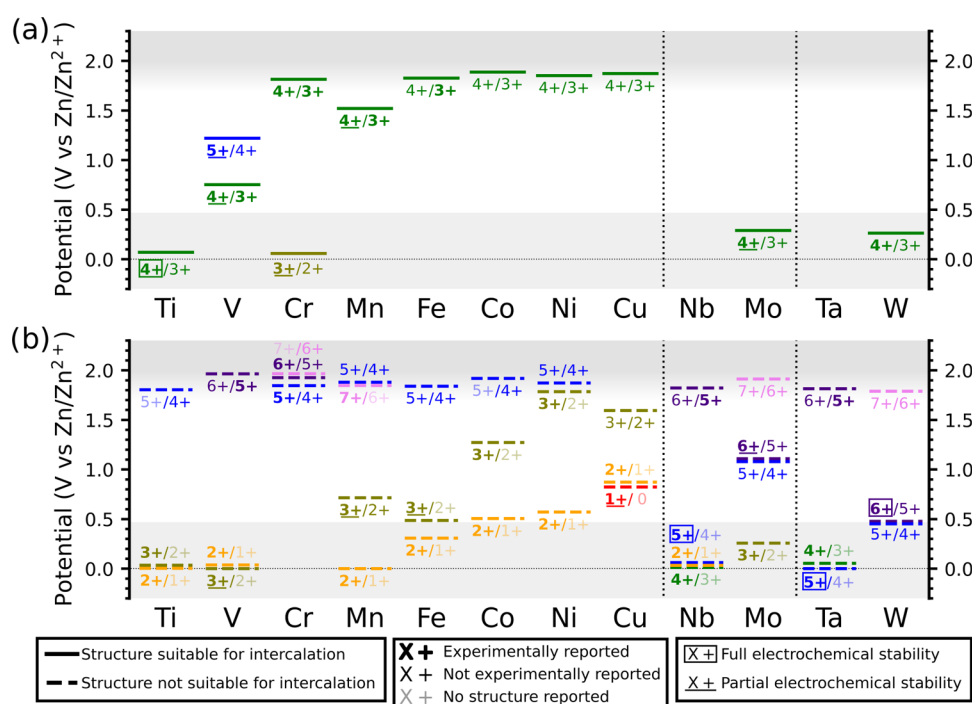


Figure 4. Zinc intercalation potential diagrams for transition metal oxide redox pairs with structures considered to be (a) suitable and (b) not suitable for intercalation. Structures considered suitable for intercalation are those identified by the Battery Explorer tool, with an example being presented for the $\text{Cr}^{4+}/\text{Cr}^{3+}$ redox pair in Figure 2a,b. The gray background delimits the calculated potentials for the HER and OER at a pH equal to 5.

calculations when obtaining the relevant thermodynamic properties.⁷²

To investigate the equilibrium electrochemical stability of the studied structures, we used experimentally obtained Pourbaix diagrams.⁷³ The Pourbaix diagram allows us to determine which phases are considered to be stable under the operating conditions of the battery, capturing the reactions (metal dissolution or solid phase change) that are anticipated to occur for those phases. In this analysis, we focused on the pH range of 3–6, which corresponds to the mildly acidic electrolytes used in RAZIBs.^{74,75} The potential window is delimited by the HER and OER. We obtained the Pourbaix diagrams using the FactSage thermochemical software,⁷⁶ assuming a concentration of the aqueous species of 0.1 M and ambient temperature. Since data for Ta were not available from the software, its diagram was created individually based on experimental data from the literature.⁷⁷

The theoretical specific capacity (in mA h g^{-1}) for each redox pair was also calculated following the equation⁷⁸

$$C_{\text{theo}} = \frac{zn_e F}{3.6W_{M_xO_y}} \quad (4)$$

where F is the Faraday constant and $W_{M_xO_y}$ is the molar mass of the host material M_xO_y .

The redox pairs considered in this study were separated into two groups to facilitate the result analysis. The first group, which will be thoroughly discussed in this article, encompasses the redox pairs for which a single electron is gained per transition metal site between the charged and discharged oxides (e.g., $4+/3+$, $2+/1+$). The second group contains the remaining redox pairs (e.g., $6+/4+$, $3+/2.5+$), for which the results will be presented in the Supporting Information (SI).

Experimental Methods. The electrochemical properties of the prepared electrodes were evaluated by using CR2032-type coin-cell batteries. Commercially available $\alpha\text{-MnO}_2$ (Vibrant Technologies), Vulcan XC-72 carbon black (Fuel Cell Store), and poly(tetrafluoroethylene) (Sigma-Aldrich) were added in a 70:20:10 ratio by weight, respectively, and dispersed in a 2:1 by volume solution of deionized water and isopropyl alcohol. The slurry was then mixed (Mazerustar KK-250S) until it was smooth, homogeneous, and flowable. Electrodes were cast onto carbon paper (AvCarb P50, Fuel Cell Stores) sheets using the doctor blade method and dried at 100 °C for 2 h. Once dried, the electrode sheet was punched into disks with a 12 mm diameter. The average mass loading of the active material on the punched electrodes was 1.5 mg cm^{-2} . The cells were assembled with a zinc foil (0.008 in., McMaster-Carr) counter electrode, glass-fiber separator (grade GF/D, Whatman), and 150 μL of 1 M ZnSO_4 aqueous electrolyte (pH = 5). The impact of the electrolyte pH on the capacity retention of the $\alpha\text{-MnO}_2$ cathode materials was also evaluated by altering the ZnSO_4 electrolyte pH before cycling. For these tests, higher mass loading electrodes of approximately 3.0 mg cm^{-2} were used, with electrolytes with pH equal to 2, 3, 4, and 5 being investigated. The electrolytes at the different pH values were obtained by dropwise addition of aliquots of 0.1 M H_2SO_4 to a 50 mL solution of 1 M ZnSO_4 under constant stirring until the desired pH was reached. The pH was measured by using a Hanna Instruments edge tablet pH meter. Galvanostatic charge and discharge testing was done using a battery testing system (NEWARE BTS4000-SV100mA) on a voltage range of 1.10–1.80 V vs Zn/Zn^{2+} with a current density of 0.1 or 1.0 A g^{-1} .

Table 1. Experimentally and Theoretically Reported Zn^{2+} Intercalation Potential for Different Transition Metal Oxides, Alongside the Zn^{2+} Intercalation Potential Predicted in This Study

material	experimental			theoretical	
	potential (V vs Zn/Zn^{2+})	conditions	electrolyte composition	potential (V vs Zn/Zn^{2+}) literature	this study
V_2O_5	1.02 ^{82,a}	20 mA g^{-1}	3.65 M ZnSO_4	1.09 ³¹	1.22
VO_2	0.78 ^{69,b}	0.1 mV s^{-1}	3 M $\text{Zn}(\text{CH}_3\text{F}_3\text{SO}_3)_2$	0.77 ³²	0.75
MnO_2	1.46 ^{83,b}	0.1 mV s^{-1}	3 M ZnSO_4 + 0.1 M MnSO_4	1.35, ⁵⁹ 1.5 ⁴⁰	1.52
Fe_2O_3	0.55 ^{46,b}	0.1 mV s^{-1}	3 M $\text{Zn}(\text{CF}_3\text{SO}_3)_2$		0.49
CuO	0.90 ^{52,a}	50 mA g^{-1}	3 M ZnSO_4		0.87
Cu_2O	0.91 ^{48,a}	100 mA g^{-1}	3 M ZnSO_4		0.82
MoO_3	0.90 ^{84,b}	20 mV s^{-1}	2 M ZnSO_4		1.10
MoO_2	0.51 ^{49,b}	0.8 mV s^{-1}	2 M $\text{Zn}(\text{CF}_3\text{SO}_3)_2$		0.29
WO_3	0.59 ^{54,b}	0.1 mV s^{-1}	2 M ZnSO_4		0.46

^aPotential plateau from the GCD plot assigned to Zn^{2+} intercalation. ^bAverage of CV peaks assigned to Zn^{2+} intercalation.

RESULTS AND DISCUSSION

To convey our findings, we employed a notation that contrasts the oxidation state of the redox active element (in this case, the transition metal ion present in the oxide) between the charged and discharged states. For example, the $4+/3+$ redox pair represents the transition between a charged oxide with the formula MO_2 (M^{4+}) and its discharged phase ZnM_2O_4 (M^{3+}). The predicted intercalation potential is shown in Figure 4 for all studied redox pairs in which a single electron is being transferred per transition metal site in the oxide (e.g., $4+/3+$, $2+/1+$). The thermodynamic properties and structures for all phases considered in this analysis are presented in the SI. Redox pairs that have similar crystal structures between the charged and discharged phases were identified with the use of the Battery Explorer tool, as explained in the Computational Methods section, and are represented in Figure 4a with solid lines. Conversely, redox pairs not captured by the Battery Explorer tool are presented in Figure 4b with dashed lines. Each redox pair has been assigned a color to facilitate the comparison between the obtained intercalation potentials for the same redox pair from different elements. Regarding the materials themselves, those that have been experimentally observed have their associated oxidation state in bold font, while regular fonts are used for structures present in the database but not experimentally obtained, and regular fonts with low opacity are used for materials with no representative structure available in the database. The experimental realization of the charged phases was confirmed through a survey of the compiled database of synthesized inorganic compounds,⁶¹ while the discharged phases were individually probed in the literature, with each structure synthesis reference presented in Tables S1 and S2 (see the SI). It is important to note that the same crystal structure phase is not necessarily used to examine both the possibility of Zn^{2+} (de)intercalation (solid or dashed line) and experimental synthesis (bold or regular font of the oxidation state), with these properties decoupled from each other in this analysis.

Regarding the electrochemical stability, an oxide is here considered fully stable if it is the only stable material on the Pourbaix diagram (Figures S3 and S4, see the SI) within the studied potential-pH window (TiO_2 , Ta_2O_5 , and WO_3 , for example). However, if a studied oxide was predicted to be stable together with other phases within the potential-pH window, this oxide was considered to be only partially stable (MnO_2 , V_2O_5 , and MoO_3 , for example). To account for

aqueous electrolyte degradation, the potentials for the OER and HER were also incorporated into the Zn^{2+} intercalation potential diagrams (Figure 4). The potentials for these electrolyte decomposition side reactions were calculated at a pH of 5, which is a typical value for RAZIB operation.^{74,75} The OER is known to require high overpotentials η applied in order to promote the formation of oxygen gas, with $\eta \geq 250$ mV at 10 mA cm^{-2} being reported for some of the leading catalysts.^{79,80} On the other hand, overpotentials around 100 mV are seen to achieve similar current densities during the HER, even without the use of precious metal catalysts.⁸¹ For this reason, when outlining the electrolyte degradation, we opted to consider the HER starting to occur at its reversible potential ($E_{\text{HER}} = 0.468$ V vs Zn/Zn^{2+} at $[\text{Zn}^{2+}] = 1$ M and pH = 5), while for the OER, an overpotential of at least 300 mV (η_{OER}) can be expected to be necessary when using the oxides studied here ($E_{\text{OER}} = 1.697$ V vs Zn/Zn^{2+} at $[\text{Zn}^{2+}] = 1$ M and pH = 5). A gray background was used on the diagrams (Figures 4 and 7) to demonstrate the potential window where the HER and the OER are expected to occur, with a gradient being applied from E_{OER} to $E_{\text{OER}} + \eta_{\text{OER}}$ to represent the expected overpotential necessary for the OER.

As can be seen in Figure 4, the predicted Zn^{2+} intercalation potential was captured for more than 50 different redox pairs with the methodology employed in this study, with more than 3 redox pairs for each element being reported. Table 1 compiles the experimental and theoretical results for the Zn^{2+} intercalation potential for different cathode materials alongside the results obtained in this study. For the Zn^{2+} intercalation potentials obtained experimentally, the experimental conditions and electrolytes used in the electrochemical tests are also shown. The experimental Zn^{2+} intercalation potentials were determined from the data of cyclic voltammetry (CV) or galvanostatic charge/discharge (GCD) experiments, with the electrochemical test considered for each material shown in Table 1. For the CV test, the Zn^{2+} intercalation potential was established from the average of the potentials of the cathodic and anodic peaks. The average of the charge and discharge plateaus in the GCD plots was used to calculate the experimental Zn^{2+} intercalation potentials from this electrochemical technique. In all cases, the CV peaks and GCD plateaus were confirmed by the authors to be assigned to Zn^{2+} intercalation and not other possible mechanisms or competing reactions. From the results shown in Table 1, reasonable agreement can be seen between the calculated theoretical

potentials and previous experimental reports, with a mean absolute error of only 0.11 V being found. For example, the intercalation potential for V_2O_5 is observed experimentally close to 1.02 V vs Zn/Zn^{2+} ^{42,82} and predicted as 1.22 V vs Zn/Zn^{2+} in this study, while for Cu_2O , an even smaller difference is observed between the experimental Zn^{2+} intercalation potential of 0.91 V vs Zn/Zn^{2+} ⁴⁸ and the theoretical of 0.82 V vs Zn/Zn^{2+} calculated here. A similar agreement is also observed for Fe_2O_3 , CuO , MoO_2 , and WO_3 .^{46,49,52,54} As presented in the introduction for this paper, previous studies have calculated the intercalation potential of Zn^{2+} in oxides through different theoretical methodologies. For the $\text{Mn}^{4+}/\text{Mn}^{3+}$ redox pair, our results are in agreement with the value around 1.5 V vs Zn/Zn^{2+} for the potential calculated by Le et al.⁵⁹ and Rubel et al.⁴⁰ Similar agreement is also seen for the Zn^{2+} intercalation potential of both $\delta\text{-V}_2\text{O}_5$ and VO_2 as differences close to 0.1 V vs Zn/Zn^{2+} are seen, which also corroborate the capability of the methodology presented here to the one previously employed in the literature.

To understand the magnitude of the potentials reported in Figure 4, the chemically preferred oxidation states for a transition metal and their variation between the charged and discharged stages must be considered. The intercalation potential (E_{Zn}) is calculated from the difference in the formation enthalpy at the convex hull ($\Delta H_{\text{f}}^{\text{ch}}$) between the discharged and charged phases (eqs 2 and 3), where the more negative the contribution from the discharge phase enthalpy, the higher the potential obtained. So, if a transition metal is at its energetically preferential oxidation state when charged and transitions to one associated with a higher enthalpy when Zn^{2+} is intercalated in its structure, the energy associated with this reaction (ΔH_{Zn}) is expectedly low in magnitude, thus a lower E_{Zn} . This trend can be seen for the $\text{Cr}^{3+}/\text{Cr}^{2+}$ redox pair in Figure 4a, where the cathode material transitions from the oxidation state where its lowest $\Delta H_{\text{f}}^{\text{ch}}$ is observed (Figure 3) to a state associated with a considerably higher formation enthalpy. Conversely, the $\text{Cr}^{4+}/\text{Cr}^{3+}$ redox pair reports a considerably higher potential as Cr^{4+} reduces to Cr^{3+} due to the highly negative value for ΔH_{Zn} associated with this reaction. Therefore, in order to avoid potentials only at the extremes, as is the case for all redox couples of Ti, Nb, and Ta, the absolute value between the differences in enthalpy from the oxidation states in the redox pair should not be high. For example, the $\Delta H_{\text{f}}^{\text{ch}}$ difference between Mo_2O_5 and MoO_3 is equal to -0.044 eV/atom, with $\text{Mo}^{6+}/\text{Mo}^{5+}$ redox pair being predicted at 1.10 V vs Zn/Zn^{2+} , while an analogous calculation for $\text{Cr}^{4+}/\text{Cr}^{3+}$ redox pair (1.83 V vs Zn/Zn^{2+}) equals -0.32 eV/atom, a considerably higher absolute value. This influence from the proximity of values for $\Delta H_{\text{f}}^{\text{ch}}$ to obtain moderate intercalation potentials can be directly attested for Mn and Mo by comparing their convex hull diagrams (Figure S1, see the SI) to the potential predicted for their redox pairs (Figure 4).

When considering the calculated intercalation potential for the same redox pair for the fourth-row transition metal elements, it is possible to notice a trend of achieving higher Zn^{2+} intercalation potentials when progressing on the periodic table from Ti to Cu (Figure 4). To analyze this trend, the intercalation potential and ionization energy⁸⁵ associated with the $4+/3+$ and $3+/2+$ redox pairs for the considered fourth-row transition metals are presented in Figure 5. The ionization energy was chosen as the parameter for this analysis as it is, by definition, the minimum energy necessary to remove an electron from an atom or ion in its gaseous form.⁸⁶ The $3+/2+$

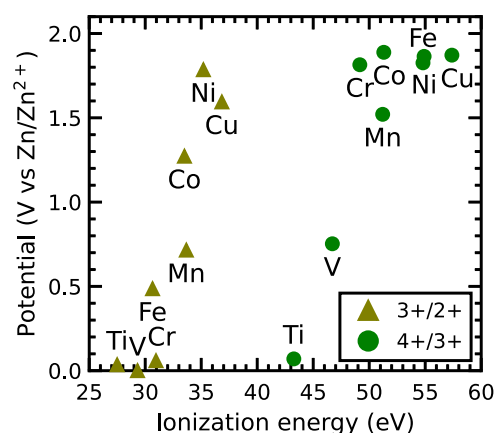


Figure 5. Relationship between the calculated Zn^{2+} intercalation potential and the associated ionization energies for selected fourth-row transition metal redox pairs.

ionization energy presented here is also known as the third ionization energy, as it is tied to the removal of the third electron from the atom, thus causing it to go from $2+$ to $3+$. From the plot presented in Figure 5, a clear trend can be seen where elements with higher ionization energies have a higher intercalation potential associated with them. As the potential increases, it indicates that Zn^{2+} insertion is predicted to be more energetically favorable, with the higher ionization energy demonstrating comparatively that the ion energetically favors being at a lower oxidation state. Therefore, the more favorable the discharged phase oxidation state, the higher the Zn^{2+} intercalation potential and ionization energy are expected to be.

In order to support the analysis of the electrochemical stability of the investigated redox pairs shown in Figure 4, we present in Figure 6 the charge–discharge curves and the capacity evolution through multiple cycles for the MnO_2 cathode at two current densities chosen to represent fast and slow charging rates. The electrochemical stability of MnO_2 , currently one of the leading materials in the literature,^{22,24,25} will be used as a baseline for comparison when evaluating new RAZIB cathode materials. First, it is important to point out the agreement in the Zn^{2+} intercalation potential for the $\text{Mn}^{4+}/\text{Mn}^{3+}$ redox pair between the theoretical prediction (~ 1.5 V vs Zn/Zn^{2+} see Figure 4a) and the experimental results shown in Figure 6a. This agreement supports the prediction capabilities of the theoretical approach applied in this study. The capacity fade for the MnO_2 cell occurs continuously during battery cycling at both investigated current densities, as evident in Figure 6b. This phenomenon has been experimentally attributed to the increase in Mn^{2+} concentration in the aqueous electrolyte during battery discharge, followed by the irregular deposition of MnO_2 during charge, which negatively affects subsequent Zn^{2+} intercalation.^{40,74,87} The susceptibility of the Mn atoms to dissolve into the electrolyte as Mn^{2+} is also supported by the analysis of its experimental Pourbaix diagram⁷⁶ (Figure S3d, see the SI), with MnO_2 being partially (un)stable within the potential and pH window relevant for RAZIB operation. Therefore, the partial electrochemical instability of the oxide material in aqueous media is determined to be directly correlated with the occurrence of capacity fade during operation as a cathode in RAZIBs. It is also important to note that the attribution of Mn^{2+} dissolution to the capacity fade has been experimentally observed to occur

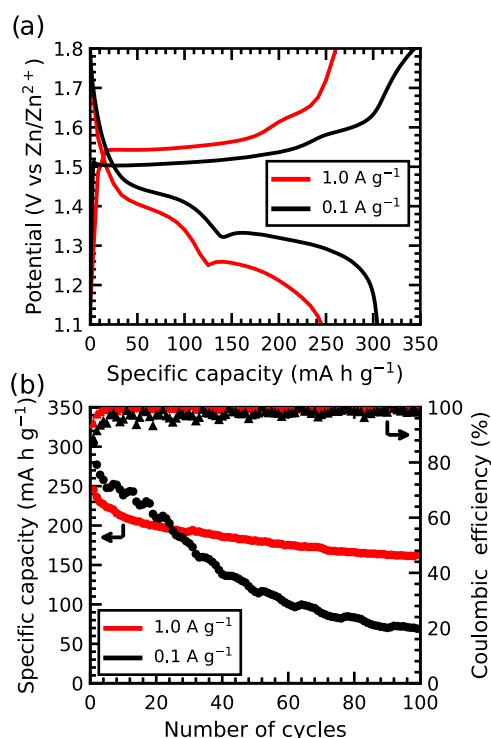


Figure 6. (a) Charge/discharge curve for the α - MnO_2 /Zn aqueous battery during the first cycle and (b) the evolution of its specific capacity through 100 cycles at two different current densities: 1.0 (red) and 0.1 (black) A g^{-1} .

independently of the MnO_2 cathode crystal structure and operating mechanism attributed to the battery system (e.g., Zn^{2+} intercalation, conversion reaction, dissolution/redeposition, and H^+ and Zn^{2+} coinserction).^{74,87–90} In this study, the Zn^{2+} intercalation mechanism was considered solely during the modeling of the battery working potential, not being factored in during the investigation of the origins of the capacity fade in the MnO_2 cathode. Therefore, the analysis of electrochemical stability and its impact on the cathode material's capacity fade is independent of the explored battery operation mechanism.

The experimentally demonstrated capacity fade shown in Figure 6b becomes more prominent when cycling at a lower current density (23% capacity retention at 0.1 A g^{-1} after 100

cycles) compared to a higher one (67% capacity retention at 1.0 A g^{-1} after 100 cycles). This is considerably detrimental to their use in grid-scale energy storage as low current densities are necessary to achieve the longer than 2 h charge/discharge cycles sought after for this application⁴ (approximately 1.4 h and 12 min cycles when cycling at 0.1 and 1.0 A g^{-1} , respectively). As the same electrochemical mechanism is expected to occur at both current densities given the similar charged/discharged profile (Figure 6a), it can be inferred that the longer cycling time at lower current density would allow for a higher extent of Mn^{2+} dissolution, resulting in a higher capacity fade. The direct correlation of higher capacity fade at lower current densities (and vice versa) has also been demonstrated in prior investigations of MnO_2 cathodes for RAZIBs.^{24,38,39} The sensitivity of capacity fade to the employed current density raises doubts about previous claims regarding the development of highly stable (greater than 90% capacity retention after more than 1000 cycles) MnO_2 cathode materials for RAZIBs in grid-scale energy storage.^{34–37}

In order to verify if the failure mechanism conclusions obtained from the experimental investigation of MnO_2 (Figure 6) would hold throughout the pH window considered in the electrochemical stability analysis, specific capacity retention tests were carried out for MnO_2 /Zn cells with different initial electrolyte pH. The results for this analysis are presented in the SI (Figure S5), with pH equal to 2, 3, 4, and 5 and current densities of 0.1 and 1.0 A g^{-1} being considered. Figure S5 shows that pH has a negligible influence on the specific capacity of MnO_2 over 50 cycles. The capacity fade observed is very similar at all pH conditions when cycled at the same current density. As discussed previously, the capacity fade for the MnO_2 cathode can be explained by referring to the Pourbaix diagram of Mn⁷⁶ (Figure S3d, see the SI). According to the diagram, Mn is predicted to dissolve into the electrolyte as Mn^{2+} during discharge since Mn^{2+} is the thermodynamically stable phase of Mn at lower potentials (less than 1.3 V vs Zn/ Zn^{2+}) and acidic pH. Therefore, for all investigated electrolyte pH conditions, the same capacity fade mechanism is expected to occur for the MnO_2 when cycled, which was confirmed by the experimental results. Once again, greater capacity fade was observed for the cells cycled at lower current density, regardless of the electrolyte pH. This allows for the conclusion that the capacity fade is not limited by the availability of

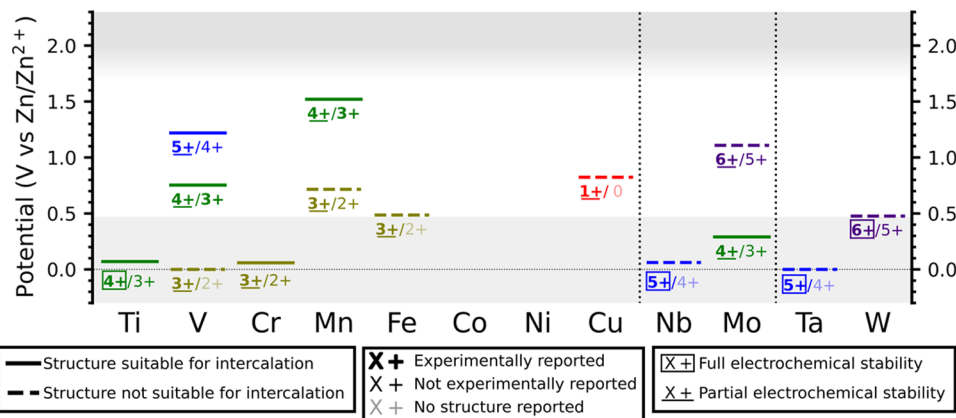


Figure 7. Zinc intercalation potential diagram for transition metal oxide redox pairs deemed to have full or partial stability from the evaluation of each transition metal Pourbaix diagram (Figures S3 and S4; see the SI). The gray background delimits the calculated potentials for the HER and OER at a pH equal to 5.

Table 2. Theoretical Specific Capacity in mA h g⁻¹ for the Investigated Redox Pairs

redox pair	element											
	Co	Cr	Cu	Fe	Mn	Mo	Nb	Ni	Ta	Ti	V	W
7+/6+		248			242	176						112
6+/5+		268				186	190		117		271	116
5+/4+	271	291		280	282	197	202	272	121	305	295	120
4+/3+	295	319	281	305	308	209	215	296	126	336	323	124
3+/2+	323	353	306	336	340	223		324		373	358	
2+/1+	358		337	373	378		246	359		420	400	
1+/0			375									

protons in the electrolyte but by the length of time the cell is allowed to cycle at the lower potentials.

Similarly to MnO₂, other materials predicted here as partially (un)stable, such as V₂O₅ and MoO₃, have also displayed considerable capacity fade when used as cathode materials in RAZIBs,^{41,45,91} with the failure mechanism behind the capacity fade for V₂O₅ and MoO₃ also being attributed to the dissolution of the transition metal into the electrolyte during cycling.^{91–95} This agreement on the capacity fade mechanism between MnO₂, V₂O₅, and MoO₃ suggests that the same conclusion realized experimentally for MnO₂ with respect to the relationship between capacity fade and electrochemical (in)stability would be arrived at if V₂O₅ or MoO₃ had been selected for experimental investigation in place of MnO₂. Taking into account the relationship between the partial electrochemical (in)stability and the capacity fade during battery operation, it is possible to infer that full electrochemical stability is crucial to have a cathode material with high capacity retention in aqueous media at practical charge rates. When analyzing the Zn²⁺ intercalation potential diagram with only the materials with full or partial stability (Figure 7), it is possible to conclude that no cathode material analyzed in this study would be expected to perform effectively as a cathode in RAZIBs. This is because all of those considered fully stable (Ti⁴⁺, Nb⁵⁺, Ta⁵⁺, W⁶⁺) have their Zn²⁺ intercalation potential at or close to the potential for the HER. However, given their full electrochemical stability, Ti⁴⁺, Nb⁵⁺, Ta⁵⁺, and W⁶⁺ can be envisioned as alloying agents in other oxide cathode materials, aiming to diminish the observed capacity fade during cycling. Additionally, all cathode materials shown in Figure 7 to be at least electrochemically partially (un)stable and report Zn²⁺ intercalation potential within the limits for the HER and OER (VO₂^{32,69}, V₂O₅,³⁰ Mn₂O₃,^{26,28} MnO₂,^{24,27} Fe₂O₃,⁴⁶ Cu₂O,⁴⁸ MoO₃⁵¹) have been previously investigated as cathodes for RAZIBs. Considering the previous experimental investigation of oxides with favorable stability and potential attributes and the extent of redox pairs investigated in this study, it is possible to conclude that a complete exploration of possible simple transition metal oxide cathodes for RAZIBs has been reached. This conclusion is in agreement with what is currently reported in the literature, where the focus is being given to improving the performance of already researched cathode materials and not to the investigation of entirely new ones.^{67,96,97} Specifically, research interest in oxides of Mn and V stands out when compared to other transition metal oxides.^{67,96,97} The reason behind this is directly linked to the fact that only these two transition metals report multiple redox pairs with partial electrochemical (in)stability in aqueous media and also appropriate Zn²⁺ intercalation potential (between the HER and the OER). Furthermore, the absence of fully stable redox pairs with Zn²⁺ intercalation potential suitable for RAZIBs

further supports the current focus of studying methods to improve the performance of Mn- and V-based oxides as cathodes for RAZIBs.

As discussed previously, all of the redox pairs with full or partial (in)stability in aqueous media have their Zn²⁺ intercalation potential at (or close to) the potential for the HER or have already been experimentally investigated. For this reason, no promising novel cathode materials to be used in RAZIBs can be proposed here. However, multiple unexplored redox pairs with high Zn²⁺ intercalation potentials (above 1.6 V vs Zn/Zn²⁺, see Figure 4), which can be of interest for nonaqueous RZIBs,^{98,99} were identified. The Cr⁴⁺/Cr³⁺ redox pair stands out as it has both phases (CrO₂/ZnCr₂O₄) previously experimentally obtained,^{61,100} as well as reporting structures that can be considered feasible for Zn²⁺ intercalation. As can be seen in Table 2, the theoretical specific capacity of the Cr⁴⁺/Cr³⁺ redox pair is also high (319 mA h g⁻¹), being comparable to that of currently researched RAZIBs cathode materials (308 and 295 mA h g⁻¹ for Mn⁴⁺/Mn³⁺ and V⁵⁺/V⁴⁺, respectively). For these reasons, Cr⁴⁺/Cr³⁺ is considered here as the main redox pair for future experimental investigation in nonaqueous RZIBs. Cr₂O₅ (Cr⁵⁺/Cr⁴⁺), CrO₃ (Cr⁶⁺/Cr⁵⁺), and ZnFe₂O₄ (Fe⁴⁺/Fe³⁺) are also proposed here for experimental study as cathode materials for RZIBs, as all three of these oxides have been previously synthesized^{61,101} and are expected to have high Zn²⁺ intercalation potentials and specific capacity (above 250 mA h g⁻¹). The Zn-containing oxides ZnNb₂O₆ (Nb⁶⁺/Nb⁵⁺) and ZnTa₂O₆ (Ta⁶⁺/Ta⁵⁺) are also recommended for future investigation, as they have also been previously synthesized¹⁰² and have high predicted Zn²⁺ intercalation potentials. However, the lower theoretical specific capacity of ZnNb₂O₆ and ZnTa₂O₆ places them at a lower position of recommendation for experimental evaluation when compared to Cr₂O₅, CrO₃, and ZnFe₂O₄. Finally, the experimentally realized⁶¹ Mn₂O₇ (Mn⁷⁺/Mn⁶⁺) and Ni₂O₃ (Ni³⁺/Ni²⁺) are also proposed for future investigation. However, different from all of the other materials being recommended here, no structure is currently reported for the discharged phases of Mn₂O₇ and Ni₂O₃.

CONCLUSIONS

A roadmap for the development of next-generation cathode materials for RZIBs was proposed based on the calculation of the Zn²⁺ intercalation potential for simple transition metal oxides. By utilization of readily available DFT-calculated thermodynamic data, more than 50 redox pairs of oxides from 12 different transition metals were investigated. The obtained results were then compared to previously reported experimental and theoretical results. The good agreement with previous experimental reports emphasizes how the applied

approach can guide the discovery of novel materials. The existence of similarly charged and discharged structures for each studied redox pair, previous reports of the synthesis of each oxide, the electrochemical stability of the cathode in a RAZIB, and the degradation of the aqueous electrolyte itself were all considered during the analysis of the results for these cathode materials. The magnitude of the calculated potentials was then explained through an analysis of the energetically favorable oxidation states for the transition element, with the trends in the potential for the same redox pair for various elements rationalized based on the associated ionization energy. Experimental investigation of the capacity retention of the MnO_2 cathode in an aqueous environment was also pursued. The capacity fade observed at slow cycling rates is attributed to a partial electrochemical instability of MnO_2 , which causes the active material to dissolve into the electrolyte during cycling. A similar electrochemical stability analysis was also pursued for the other studied oxides, revealing multiple currently studied cathode materials that were predicted to suffer from capacity fade due to the same failure mechanism. The simple oxides of Ti^{4+} , Nb^{5+} , Ta^{5+} , and W^{6+} were also identified from the electrochemical stability analysis as fully stable transition metal oxides within the potential and pH range observed during the operation of RAZIBs. The full stability seen for these oxides granted these transition metals to be proposed as alloying elements in other host structures to develop RAZIBs cathode materials with higher stability/capacity retention. Finally, CrO_2 , CrO_3 , ZnFe_2O_4 , ZnNb_2O_6 , and other yet unexplored materials were proposed as cathodes for nonaqueous RZIBs, with all of these materials displaying high Zn^{2+} intercalation potential (1.7–1.9 V vs Zn/Zn^{2+}). Based on the findings of this article, a direction for future experimental investigation of cathode materials for RZIBs was proposed, which aims to expedite the development of this battery technology.

■ ASSOCIATED CONTENT

SI Supporting Information

The Supporting Information is available free of charge at <https://pubs.acs.org/doi/10.1021/acs.jpcc.4c03418>.

Convex hull diagrams for Mn and Mo; zinc intercalation potential diagram; experimentally obtained Pourbaix diagrams; experimental MnO_2 capacity retention results for different initial pH and tables with the thermodynamic properties for all of the materials used in this study; references cited within the SI^{65,76,77,100–127} (PDF)

■ AUTHOR INFORMATION

Corresponding Author

Caio Miranda Miliante – Department of Materials Science and Engineering, McMaster University, Hamilton, Ontario L8S 4L8, Canada; orcid.org/0000-0002-5199-0716; Email: miliante@mcmaster.ca

Authors

Storm Gourley – Department of Chemical Engineering, McMaster University, Hamilton, Ontario L8S 4L8, Canada
Brian D. Adams – Salient Energy Inc., Dartmouth, Nova Scotia B3B 1C4, Canada

Drew Higgins – Department of Chemical Engineering, McMaster University, Hamilton, Ontario L8S 4L8, Canada; orcid.org/0000-0002-0585-2670

Oleg Rubel – Department of Materials Science and Engineering, McMaster University, Hamilton, Ontario L8S 4L8, Canada; orcid.org/0000-0001-5104-5602

Complete contact information is available at:

<https://pubs.acs.org/10.1021/acs.jpcc.4c03418>

Notes

The authors declare the following competing financial interest(s): Brian D. Adams is a cofounder and partial owner of Salient Energy Inc.

■ ACKNOWLEDGMENTS

This work was supported by Salient Energy and the NSERC Alliance program.

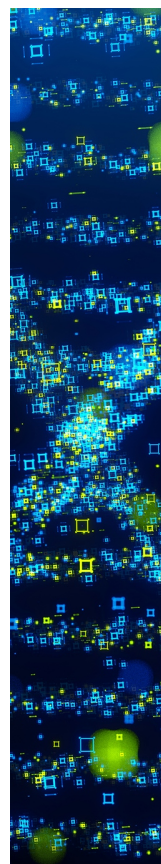
■ REFERENCES

- (1) Barton, J. P.; Infield, D. G. Energy storage and its use with intermittent renewable energy. *IEEE Trans. Energy Convers.* **2004**, *19*, 441–448.
- (2) Evans, A.; Strezov, V.; Evans, T. J. Assessment of utility energy storage options for increased renewable energy penetration. *Renewable Sustainable Energy Rev.* **2012**, *16*, 4141–4147.
- (3) Sayed, E. T.; Olabi, A. G.; Alami, A. H.; Radwan, A.; Mdallal, A.; Rezk, A.; Abdelkareem, M. A. Renewable energy and energy storage systems. *Energies* **2023**, *16*, No. 1415.
- (4) Gourley, S. W.; Brown, R.; Adams, B. D.; Higgins, D. Zinc-ion batteries for stationary energy storage. *Joule* **2023**, *7*, 1415–1436.
- (5) Luo, X.; Wang, J.; Dooner, M.; Clarke, J. Overview of current development in electrical energy storage technologies and the application potential in power system operation. *Appl. Energy* **2015**, *137*, 511–536.
- (6) Schoenfisch, M.; Dasgupta, A. Grid-Scale Storage, 2023. <https://www.iea.org/energy-system/electricity/grid-scale-storage> (accessed Dec, 2023).
- (7) IRENA. Innovation landscape Brief: Utility-Scale Batteries, 2019. https://www.irena.org/-/media/Files/IRENA/Agency/Publication/2019/Sep/IRENA_Utility-scale-batteries_2019.pdf (accessed Dec, 2023).
- (8) Frazier, A. W.; Cole, W.; Denholm, P.; Machen, S.; Gates, N.; Blair, N. *Storage Futures Study: Economic Potential of Diurnal Storage in the US Power Sector*; National Renewable Energy Lab (NREL), 2021. <https://www.nrel.gov/docs/fy21osti/77449.pdf>.
- (9) Park, M. J.; Yaghoobnejad Asl, H.; Manthiram, A. Multivalent-ion versus proton insertion into battery electrodes. *ACS Energy Lett.* **2020**, *5*, 2367–2375.
- (10) Blanc, L. E.; Kundu, D.; Nazar, L. F. Scientific challenges for the implementation of Zn-ion batteries. *Joule* **2020**, *4*, 771–799.
- (11) Fan, L.; Ma, R.; Wang, J.; Yang, H.; Lu, B. An ultrafast and highly stable potassium-organic battery. *Adv. Mater.* **2018**, *30*, No. 1805486.
- (12) Pan, Z.; Liu, X.; Yang, J.; Li, X.; Liu, Z.; Loh, X. J.; Wang, J. Aqueous rechargeable multivalent metal-ion batteries: advances and challenges. *Adv. Energy Mater.* **2021**, *11*, No. 2100608.
- (13) Zhang, N.; Chen, X.; Yu, M.; Niu, Z.; Cheng, F.; Chen, J. Materials chemistry for rechargeable zinc-ion batteries. *Chem. Soc. Rev.* **2020**, *49*, 4203–4219.
- (14) Zeng, X.; Hao, J.; Wang, Z.; Mao, J.; Guo, Z. Recent progress and perspectives on aqueous Zn-based rechargeable batteries with mild aqueous electrolytes. *Energy Storage Mater.* **2019**, *20*, 410–437.
- (15) Glatz, H.; Tervoort, E.; Kundu, D. Unveiling critical insight into the Zn metal anode cyclability in mildly acidic aqueous electrolytes: implications for aqueous zinc batteries. *ACS Appl. Mater. Interfaces* **2020**, *12*, 3522–3530.

- (16) Yang, J.; Yin, B.; Sun, Y.; Pan, H.; Sun, W.; Jia, B.; Zhang, S.; Ma, T. Zinc anode for mild aqueous zinc-ion batteries: challenges, strategies, and perspectives. *Nano-Micro Lett.* **2022**, *14*, No. 42.
- (17) Cabana, J.; Monconduit, L.; Larcher, D.; Palacin, M. R. Beyond intercalation-based Li-ion batteries: The state of the art and challenges of electrode materials reacting through conversion reactions. *Adv. Mater.* **2010**, *22*, E170–E192.
- (18) Ge, H.; Qin, L.; Zhang, B.; Jiang, L.; Tang, Y.; Lu, B.; Tian, S.; Zhou, J. An ionically cross-linked composite hydrogel electrolyte based on natural biomacromolecules for sustainable zinc-ion batteries. *Nanoscale Horiz.* **2024**, *9*, 1514–1521.
- (19) Li, J.; Liu, Z.; Han, S.; Zhou, P.; Lu, B.; Zhou, J.; Zeng, Z.; Chen, Z.; Zhou, J. Hetero nucleus growth stabilizing zinc anode for high-biosecurity zinc-ion batteries. *Nano-Micro Lett.* **2023**, *15*, No. 237.
- (20) Chao, D.; Zhou, W.; Xie, F.; Ye, C.; Li, H.; Jaroniec, M.; Qiao, S.-Z. Roadmap for advanced aqueous batteries: from design of materials to applications. *Sci. Adv.* **2020**, *6*, No. eaba4098.
- (21) Zhong, Y.; Xie, X.; Zeng, Z.; Lu, B.; Chen, G.; Zhou, J. Triple-function hydrated eutectic electrolyte for enhanced aqueous zinc batteries. *Angew. Chem.* **2023**, *62*, No. e202310577.
- (22) Selvakumaran, D.; Pan, A.; Liang, S.; Cao, G. A review on recent developments and challenges of cathode materials for rechargeable aqueous Zn-ion batteries. *J. Mater. Chem. A* **2019**, *7*, 18209–18236.
- (23) Song, M.; Tan, H.; Chao, D.; Fan, H. J. Recent advances in Zn-ion batteries. *Adv. Funct. Mater.* **2018**, *28*, No. 1802564.
- (24) Pan, H.; Shao, Y.; Yan, P.; Cheng, Y.; Han, K. S.; Nie, Z.; Wang, C.; Yang, J.; Li, X.; Bhattacharya, P.; et al. Reversible aqueous zinc/manganese oxide energy storage from conversion reactions. *Nat. Energy* **2016**, *1*, No. 16039.
- (25) Wu, D.; Housel, L. M.; Kim, S. J.; Sadique, N.; Quilty, C. D.; Wu, L.; Tapper, R.; Nicholas, S. L.; Ehrlich, S.; Zhu, Y.; et al. Quantitative temporally and spatially resolved X-ray fluorescence microprobe characterization of the manganese dissolution-deposition mechanism in aqueous Zn/ α -MnO₂ batteries. *Energy Environ. Sci.* **2020**, *13*, 4322–4333.
- (26) Hou, Q.; Ivey, D. G. An investigation into the charge storage mechanism and cycling performance of Mn₂O₃ as the cathode material for zinc-ion batteries. *Batteries Supercaps* **2022**, *5*, No. e202200190.
- (27) Tran, T. N. T.; Jin, S.; Cuisinier, M.; Adams, B. D.; Ivey, D. G. Reaction mechanisms for electrolytic manganese dioxide in rechargeable aqueous zinc-ion batteries. *Sci. Rep.* **2021**, *11*, No. 20777.
- (28) Jiang, B.; Xu, C.; Wu, C.; Dong, L.; Li, J.; Kang, F. Manganese sesquioxide as cathode material for multivalent zinc ion battery with high capacity and long cycle life. *Electrochim. Acta* **2017**, *229*, 422–428.
- (29) Zhu, C.; Fang, G.; Zhou, J.; Guo, J.; Wang, Z.; Wang, C.; Li, J.; Tang, Y.; Liang, S. Binder-free stainless steel@Mn₃O₄ nanoflower composite: a high-activity aqueous zinc-ion battery cathode with high-capacity and long-cycle-life. *J. Mater. Chem. A* **2018**, *6*, 9677–9683.
- (30) Zhao, D.; Wang, X.; Zhang, W.; Zhang, Y.; Lei, Y.; Huang, X.; Zhu, Q.; Liu, J. Unlocking the capacity of vanadium oxide by atomically thin graphene-analogous V₂O₅·nH₂O in aqueous Zinc-ion batteries. *Adv. Funct. Mater.* **2023**, *33*, No. 2211412.
- (31) Gautam, G. S.; Canepa, P.; Malik, R.; Liu, M.; Persson, K.; Ceder, G. First-principles evaluation of multi-valent cation insertion into orthorhombic V₂O₅. *Chem. Commun.* **2015**, *51*, 13619–13622.
- (32) Zhu, K.; Wu, T.; Sun, S.; van den Bergh, W.; Stefiak, M.; Huang, K. Synergistic H⁺/Zn²⁺ dual ion insertion mechanism in high-capacity and ultra-stable hydrated VO₂ cathode for aqueous Zn-ion batteries. *Energy Storage Mater.* **2020**, *29*, 60–70.
- (33) Zhao, Y.; Zhu, Y.; Zhang, X. Challenges and perspectives for manganese-based oxides for advanced aqueous zinc-ion batteries. *InfoMat* **2020**, *2*, 237–260.
- (34) Wu, B.; Zhang, G.; Yan, M.; Xiong, T.; He, P.; He, L.; Xu, X.; Mai, L. Graphene scroll-coated α -MnO₂ nanowires as high-performance cathode materials for aqueous Zn-ion battery. *Small* **2018**, *14*, No. 1703850.
- (35) Wang, H.; Liang, M.; Gao, J.; Ma, C.; He, Z.; Zhao, Y.; Miao, Z. Robust structural stability of flower-like δ -MnO₂ as cathode for aqueous zinc ion battery. *Colloids Surf., A* **2022**, *643*, No. 128804.
- (36) Wang, J.; Wang, J.-G.; Liu, H.; Wei, C.; Kang, F. Zinc ion stabilized MnO₂ nanospheres for high capacity and long lifespan aqueous zinc-ion batteries. *J. Mater. Chem. A* **2019**, *7*, 13727–13735.
- (37) Xu, X.; Chen, Y.; Li, W.; Yin, R.; Zheng, D.; Niu, X.; Dai, X.; Shi, W.; Liu, W.; Wu, F.; et al. Achieving ultralong-cycle zinc-ion battery via synergistically electronic and structural regulation of a MnO₂ nanocrystal–carbon hybrid framework. *Small* **2023**, *19*, No. 2207517.
- (38) Tang, H.; Chen, W.; Li, N.; Hu, Z.; Xiao, L.; Xie, Y.; Xi, L.; Ni, L.; Zhu, Y. Layered MnO₂ nanodots as high-rate and stable cathode materials for aqueous zinc-ion storage. *Energy Storage Mater.* **2022**, *48*, 335–343.
- (39) Wang, J.; Wang, J.-G.; Liu, H.; You, Z.; Li, Z.; Kang, F.; Wei, B. A highly flexible and lightweight MnO₂/graphene membrane for superior zinc-ion batteries. *Adv. Funct. Mater.* **2021**, *31*, No. 2007397.
- (40) Rubel, O.; Tran, T. N. T.; Gourley, S.; Anand, S.; Bommel, A. V.; Adams, B. D.; Ivey, D. G.; Higgins, D. Electrochemical stability of ZnMn₂O₄: understanding Zn-ion rechargeable battery capacity and degradation. *J. Phys. Chem. C* **2022**, *126*, 10957–10967.
- (41) Xing, Z.; Xu, G.; Han, J.; Chen, G.; Lu, B.; Liang, S.; Zhou, J. Facing the capacity fading of vanadium-based zinc-ion batteries. *Trends Chem.* **2023**, *5*, 380–392.
- (42) Li, Y.; Huang, Z.; Kalambate, P. K.; Zhong, Y.; Huang, Z.; Xie, M.; Shen, Y.; Huang, Y. V₂O₅ nanopaper as a cathode material with high capacity and long cycle life for rechargeable aqueous zinc-ion battery. *Nano Energy* **2019**, *60*, 752–759.
- (43) Kundu, D.; Adams, B. D.; Duffort, V.; Vajargah, S. H.; Nazar, L. F. A high-capacity and long-life aqueous rechargeable zinc battery using a metal oxide intercalation cathode. *Nat. Energy* **2016**, *1*, No. 16119.
- (44) Li, C.; Jin, S.; Archer, L. A.; Nazar, L. F. Toward practical aqueous zinc-ion batteries for electrochemical energy storage. *Joule* **2022**, *6*, 1733–1738.
- (45) Liu, W.; Hao, J.; Xu, C.; Mou, J.; Dong, L.; Jiang, F.; Kang, Z.; Wu, J.; Jiang, B.; Kang, F. Investigation of zinc ion storage of transition metal oxides, sulfides, and borides in zinc ion battery systems. *Chem. Commun.* **2017**, *53*, 6872–6874.
- (46) Duan, J.; Ji, K.; Min, L.; Zhang, Y.; Yang, T.; Chen, M.; Wang, C. Hybrid electrolyte-mediated nano-scaled γ -Fe₂O₃ cathode for emerging aqueous zinc battery. *Electrochim. Acta* **2021**, *390*, No. 138883.
- (47) Xu, W.; Zhao, K.; Wang, Y. Electrochemical activated MoO₃/Mo₂N heterostructured nanobelts as superior zinc rechargeable battery cathode. *Energy Storage Mater.* **2018**, *15*, 374–379.
- (48) Wu, J.; Meng, J.; Yang, Z.; Chen, H.; Rong, Y.; Deng, L.; Fu, Z. Energy storage mechanism and electrochemical performance of Cu₂O/rGO as advanced cathode for aqueous zinc ion batteries. *J. Alloys Compd.* **2022**, *895*, No. 162653.
- (49) Zhou, Z.; Han, M.; Sun, Y.; Cui, Y.; El-khodary, S. A.; Ng, D. H.; Lian, J.; Ma, J. Zinc-ion and proton as joint charge carriers of S-MoO₃ for high-capacity aqueous zinc-ion batteries. *Adv. Funct. Mater.* **2024**, *34*, No. 2308834.
- (50) Songmueang, K.; Zhang, D.; Cao, J.; Zhang, X.; Kheawhom, S.; Sriprachubwong, C.; Tuantranont, A.; Wangyao, P.; Qin, J. Flower-like W/VO₃ as a novel cathode for aqueous zinc-ion batteries. *Chem. Commun.* **2021**, *57*, 7549–7552.
- (51) Fang, Z.; Liu, C.; Li, X.; Peng, L.; Ding, W.; Guo, X.; Hou, W. Systematic modification of MoO₃-based cathode by the intercalation engineering for high-performance aqueous zinc-ion batteries. *Adv. Funct. Mater.* **2023**, *33*, No. 2210010.
- (52) Meng, J.; Yang, Z.; Chen, L.; Qin, H.; Cui, F.; Jiang, Y.; Zeng, X. Energy storage performance of CuO as a cathode material for aqueous zinc ion battery. *Mater. Today Energy* **2020**, *15*, No. 100370.

- (53) Ma, L.; Chen, S.; Li, H.; Ruan, Z.; Tang, Z.; Liu, Z.; Wang, Z.; Huang, Y.; Pei, Z.; Zapien, J. A.; Zhi, C. Initiating a mild aqueous electrolyte $\text{Co}_3\text{O}_4/\text{Zn}$ battery with 2.2 V-high voltage and 5000-cycle lifespan by a Co(III) rich-electrode. *Energy Environ. Sci.* **2018**, *11*, 2521–2530.
- (54) Li, S.; Zhang, Z.; Wu, J.; Guo, X.; Chen, Y.; Wang, C.; Yu, F.; Wang, Z.; Li, D.; Chen, Y. Stable $\text{Zn}-\text{WO}_3$ battery with a ZnCl_2 water-in-salt electrolyte. *J. Power Sources* **2023**, *560*, No. 232691.
- (55) Chevrier, V. L.; Ong, S. P.; Armiento, R.; Chan, M. K. Y.; Ceder, G. Hybrid density functional calculations of redox potentials and formation energies of transition metal compounds. *Phys. Rev. B* **2010**, *82*, No. 075122.
- (56) Aydinol, M. K.; Kohan, A. F.; Ceder, G.; Cho, K.; Joannopoulos, J. Ab initio study of lithium intercalation in metal oxides and metal dichalcogenides. *Phys. Rev. B* **1997**, *56*, 1354–1365.
- (57) Zhang, Z.; Zhang, X.; Zhao, X.; Yao, S.; Chen, A.; Zhou, Z. Computational screening of layered materials for multivalent ion batteries. *ACS Omega* **2019**, *4*, 7822–7828.
- (58) Liu, M.; Rong, Z.; Malik, R.; Canepa, P.; Jain, A.; Ceder, G.; Persson, K. A. Spinel compounds as multivalent battery cathodes: a systematic evaluation based on ab initio calculations. *Energy Environ. Sci.* **2015**, *8*, 964–974.
- (59) Le, T.; Sadique, N.; Housel, L. M.; Poyraz, A. S.; Takeuchi, E. S.; Takeuchi, K. J.; Marschilok, A. C.; Liu, P. Discharging behavior of hollandite $\alpha\text{-MnO}_2$ in a hydrated zinc-ion battery. *ACS Appl. Mater. Interfaces* **2021**, *13*, 59937–59949.
- (60) Perdew, J. P.; Burke, K.; Ernzerhof, M. Generalized gradient approximation made simple. *Phys. Rev. Lett.* **1996**, *77*, 3865–3868.
- (61) ref 128, pp 4–1–4–12.
- (62) Padhi, A. K. Mapping Redox Energies of Electrode Materials for Lithium Batteries. Ph.D. Thesis, The University of Texas at Austin, 1997.
- (63) Liu, D.; Zhu, W.; Trottier, J.; Gagnon, C.; Barray, F.; Guerfi, A.; Mauger, A.; Groult, H.; Julien, C.; Goodenough, J.; Zaghib, K. Spinel materials for high-voltage cathodes in Li-ion batteries. *RSC Adv.* **2014**, *4*, 154–167.
- (64) Goodenough, J. B.; Kim, Y. Challenges for rechargeable Li batteries. *Chem. Mater.* **2010**, *22*, 587–603.
- (65) Jain, A.; Ong, S. P.; Hautier, G.; Chen, W.; Richards, W. D.; Dacek, S.; Cholia, S.; Gunter, D.; Skinner, D.; Ceder, G.; Persson, K. A. Commentary: The Materials Project: A materials genome approach to accelerating materials innovation. *APL Mater.* **2013**, *1*, No. 011002.
- (66) Ong, S. P.; Wang, L.; Kang, B.; Ceder, G. Li-Fe-P-O₂ phase diagram from first principles calculations. *Chem. Mater.* **2008**, *20*, 1798–1807.
- (67) Li, G.; Sun, L.; Zhang, S.; Zhang, C.; Jin, H.; Davey, K.; Liang, G.; Liu, S.; Mao, J.; Guo, Z. Developing cathode materials for aqueous zinc ion batteries: challenges and practical prospects. *Adv. Funct. Mater.* **2024**, *34*, No. 2301291.
- (68) Zhou, T.; Zhu, L.; Xie, L.; Han, Q.; Yang, X.; Chen, L.; Wang, G.; Cao, X. Cathode materials for aqueous zinc-ion batteries: a mini review. *J. Colloid Interface Sci.* **2022**, *605*, 828–850.
- (69) Cui, F.; Zhao, J.; Zhang, D.; Fang, Y.; Hu, F.; Zhu, K. $\text{VO}_2(\text{B})$ nanobelts and reduced graphene oxides composites as cathode materials for low-cost rechargeable aqueous zinc ion batteries. *Chem. Eng. J.* **2020**, *390*, No. 124118.
- (70) Jain, A.; Hautier, G.; Moore, C. J.; Ong, S. P.; Fischer, C. C.; Mueller, T.; Persson, K. A.; Ceder, G. A high-throughput infrastructure for density functional theory calculations. *Comput. Mater. Sci.* **2011**, *50*, 2295–2310.
- (71) Jain, A.; Hautier, G.; Ong, S. P.; Moore, C. J.; Fischer, C. C.; Persson, K. A.; Ceder, G. Formation enthalpies by mixing GGA and GGA + *U* calculations. *Phys. Rev. B* **2011**, *84*, No. 045115.
- (72) Wang, A.; Kingsbury, R.; McDermott, M.; Horton, M.; Jain, A.; Ong, S. P.; Dwarknath, S.; Persson, K. A. A framework for quantifying uncertainty in DFT energy corrections. *Sci. Rep.* **2021**, *11*, No. 15496.
- (73) ref 129, pp 29–50.
- (74) Bischoff, C. F.; Fitz, O. S.; Burns, J.; Bauer, M.; Gentischer, H.; Birke, K. P.; Henning, H.-M.; Biro, D. Revealing the local pH value changes of acidic aqueous zinc ion batteries with a manganese dioxide electrode during cycling. *J. Electrochem. Soc.* **2020**, *167*, No. 020545.
- (75) Rodríguez-Pérez, I. A.; Chang, H. J.; Fayette, M.; Sivakumar, B. M.; Choi, D.; Li, X.; Reed, D. Mechanistic investigation of redox processes in $\text{Zn}-\text{MnO}_2$ battery in mild aqueous electrolytes. *J. Mater. Chem. A* **2021**, *9*, 20766–20775.
- (76) Bale, C. W.; Chartrand, P.; Degterov, S.; Eriksson, G.; Hack, K.; Mahfoud, R. B.; Melançon, J.; Pelton, A.; Petersen, S.; et al. FactSage thermochemical software and databases, 2010–2016. *Calphad* **2016**, *54*, 35–53.
- (77) ref 129, pp 251–255.
- (78) Wu, X.; Kang, F.; Duan, W.; Li, J. Density functional theory calculations: a powerful tool to simulate and design high-performance energy storage and conversion materials. *Prog. Nat. Sci.: Mater. Int.* **2019**, *29*, 247–255.
- (79) Wang, C.; Schechter, A.; Feng, L. Iridium-based catalysts for oxygen evolution reaction in acidic media: mechanism, catalytic promotion effects and recent progress. *Nano Res. Energy* **2023**, *2*, No. e9120056.
- (80) Yu, H.; Ke, J.; Shao, Q. Two dimensional Ir-based catalysts for acidic OER. *Small* **2023**, *19*, No. 2304307.
- (81) Zhao, G.; Rui, K.; Dou, S. X.; Sun, W. Heterostructures for electrochemical hydrogen evolution reaction: a review. *Adv. Funct. Mater.* **2018**, *28*, No. 1803291.
- (82) Qin, H.; Chen, L.; Wang, L.; Chen, X.; Yang, Z. V_2O_5 hollow spheres as high rate and long life cathode for aqueous rechargeable zinc ion batteries. *Electrochim. Acta* **2019**, *306*, 307–316.
- (83) Jing, F.; Pei, J.; Zhou, Y.; Shang, Y.; Yao, S.; Liu, S.; Chen, G. High-performance reversible aqueous zinc-ion battery based on Zn^{2+} pre-intercalation alpha-manganese dioxide nanowires/carbon nanotubes. *J. Colloid Interface Sci.* **2022**, *609*, 557–565.
- (84) He, Y.; Tang, H.; Huang, Y.; Chen, K.; Wang, G.; Zheng, D.; Xu, W.; Wang, F.; Lu, X. Valence modulation and morphological engineering of MoO_3 as high-performance cathode for aqueous zinc ion batteries. *Electrochim. Acta* **2023**, *465*, No. 142988.
- (85) ref 128, pp 2–2–2–5.
- (86) Matsumoto, P. S. Trends in ionization energy of transition-metal elements. *J. Chem. Educ.* **2005**, *82*, 1660.
- (87) Lee, B.; Seo, H. R.; Lee, H. R.; Yoon, C. S.; Kim, J. H.; Chung, K. Y.; Cho, B. W.; Oh, S. H. Critical role of pH evolution of electrolyte in the reaction mechanism for rechargeable zinc batteries. *ChemSusChem* **2016**, *9*, 2948–2956.
- (88) Alfaruqi, M. H.; Islam, S.; Putro, D. Y.; Mathew, V.; Kim, S.; Jo, J.; Kim, S.; Sun, Y.-K.; Kim, K.; Kim, J. Structural transformation and electrochemical study of layered MnO_2 in rechargeable aqueous zinc-ion battery. *Electrochim. Acta* **2018**, *276*, 1–11.
- (89) Liu, W.; Zhang, X.; Huang, Y.; Jiang, B.; Chang, Z.; Xu, C.; Kang, F. $\beta\text{-MnO}_2$ with proton conversion mechanism in rechargeable zinc ion battery. *J. Energy Chem.* **2021**, *56*, 365–373.
- (90) Liao, Y.; Chen, H.-C.; Yang, C.; Liu, R.; Peng, Z.; Cao, H.; Wang, K. Unveiling performance evolution mechanisms of MnO_2 polymorphs for durable aqueous zinc-ion batteries. *Energy Storage Mater.* **2022**, *44*, 508–516.
- (91) He, X.; Zhang, H.; Zhao, X.; Zhang, P.; Chen, M.; Zheng, Z.; Han, Z.; Zhu, T.; Tong, Y.; Lu, X. Stabilized molybdenum trioxide nanowires as novel ultrahigh-capacity cathode for rechargeable zinc ion battery. *Adv. Sci.* **2019**, *6*, No. 1900151.
- (92) Kim, Y.; Park, Y.; Kim, M.; Lee, J.; Kim, K. J.; Choi, J. W. Corrosion as the origin of limited lifetime of vanadium oxide-based aqueous zinc ion batteries. *Nat. Commun.* **2022**, *13*, No. 2371.
- (93) Zhu, K.; Wu, T.; Huang, K. Understanding the dissolution and phase transformation mechanisms in aqueous $\text{Zn}/\alpha\text{-V}_2\text{O}_5$ batteries. *Chem. Mater.* **2021**, *33*, 4089–4098.
- (94) Li, W.; Jiang, W.; Zhu, K.; Wang, Z.; Xie, W.; Yang, H.; Ma, M.; Yang, W. Unlocking the performance degradation of vanadium-based cathodes in aqueous zinc-ion batteries. *Chem. Eng. J.* **2024**, *496*, No. 153786.

- (95) Wang, L.; Yan, S.; Quilty, C. D.; Kuang, J.; Dunkin, M. R.; Ehrlich, S. N.; Ma, L.; Takeuchi, K. J.; Takeuchi, E. S.; Marschilok, A. C. Achieving stable molybdenum oxide cathodes for aqueous zinc-ion batteries in water-in-salt electrolyte. *Adv. Mater. Interfaces* **2021**, 8, No. 2002080.
- (96) Xu, Y.; Zhang, G.; Liu, J.; Zhang, J.; Wang, X.; Pu, X.; Wang, J.; Yan, C.; Cao, Y.; Yang, H.; et al. Recent advances on challenges and strategies of manganese dioxide cathodes for aqueous zinc-ion batteries. *Energy Environ. Mater.* **2023**, 6, No. e12575.
- (97) Qiu, Y.; Yan, Z.; Sun, Z.; Guo, Z.; Liu, H.; Du, B.; Tian, S.; Wang, P.; Ding, H.; Qian, L. Vanadium oxide-based cathode materials for aqueous zinc-ion batteries: energy storage mechanism and design strategy. *Inorganics* **2023**, 11, No. 118.
- (98) Kao-ian, W.; Mohamad, A. A.; Liu, W.-R.; Pornprasertsuk, R.; Siwamogsatham, S.; Kheawhom, S. Stability enhancement of zinc-ion batteries using non-aqueous electrolytes. *Batteries Supercaps* **2022**, 5, No. e202100361.
- (99) Pathak, P. K.; Kumar, N.; Ahn, H.; Salunkhe, R. R. Spinel zinc manganate-based high-capacity and high-stability non-aqueous zinc-ion batteries. *J. Mater. Chem. A* **2023**, 11, 25595–25604.
- (100) Kemei, M. C.; Barton, P. T.; Moffitt, S. L.; Gaultois, M. W.; Kurzman, J. A.; Seshadri, R.; Suchomel, M. R.; Kim, Y.-I. Crystal structures of spin-Jahn-Teller-ordered MgCr_2O_4 and ZnCr_2O_4 . *J. Phys.: Condens. Matter* **2013**, 25, No. 326001.
- (101) Levy, D.; Pavese, A.; Hanfland, M. Phase transition of synthetic zinc ferrite spinel (ZnFe_2O_4) at high pressure, from synchrotron X-ray powder diffraction. *Phys. Chem. Miner.* **2000**, 27, 638–644.
- (102) Waburg, M.; Müller-Buschbaum, H. ZnTa_2O_6 , ein neuer Vertreter des tri- α - PbO_2 -Typs (mit ergänzenden Daten über ZnNb_2O_6). *Z. Anorg. Allg. Chem.* **1984**, 508, 55–60.
- (103) Reehuis, M.; Krimmel, A.; Büttgen, N.; Loidl, A.; Prokofiev, A. Crystallographic and magnetic structure of ZnV_2O_4 : structural phase transition due to spin-driven Jahn-Teller distortions. *Eur. Phys. J. B* **2003**, 35, 311–316.
- (104) Fong, C.; Kennedy, B.; Elcombe, M. A powder neutron diffraction study of λ and γ manganese dioxide and of LiMn_2O_4 . *Z. Kristallogr.—Cryst. Mater.* **1994**, 209, 941–945.
- (105) McAndrew, J. Observations on hydrohetaerolite. *Am. Mineral.* **1956**, 41, 268–275.
- (106) Abrahams, S. C. Magnetic and crystal structure of titanium sesquioxide. *Phys. Rev.* **1963**, 130, 2230.
- (107) Watanabé, D.; Castles, J.; Jostsons, A.; Malin, A. The ordered structure of TiO . *Acta Crystallogr.* **1967**, 23, 307–313.
- (108) Andreetti, G. D.; Calestani, G.; Montenero, A. Refinement of the crystal structure of ZnV_2O_6 . *Z. Kristallogr.—Cryst. Mater.* **1984**, 168, 53–58.
- (109) Nakhal, S.; Hermes, W.; Ressler, T.; Poettgen, R.; Lerch, M. Synthesis, crystal structure and magnetic properties of bixbyite-type vanadium oxide nitrides. *Z. Naturforsch. B* **2009**, 64, 281–286.
- (110) Dufek, V.; Petru, F.; Brožek, V. Über sauerstoff-haltige Verbindungen vom strukturtyp B1 der ersten vier übergangsmetalle. *Monatsh. Chem.* **1967**, 98, 2424–2430.
- (111) Stephens, J. S.; Cruickshank, D. The crystal structure of $(\text{CrO}_3)_\infty$. *Acta Crystallogr., Sect. B: Struct. Crystallogr. Cryst. Chem.* **1970**, 26, 222–226.
- (112) Hill, A. H.; Harrison, A.; Dickinson, C.; Zhou, W.; Kockelmann, W. Crystallographic and magnetic studies of mesoporous eskolaite, Cr_2O_3 . *Microporous Mesoporous Mater.* **2010**, 130, 280–286.
- (113) Simon, A.; Dronskowski, R.; Krebs, B.; Hettich, B. Die kristallstruktur von Mn_2O_7 . *Angew. Chem.* **1987**, 99, 160–161.
- (114) Cockayne, E.; Levin, I.; Wu, H.; Llobet, A. Magnetic structure of bixbyite α - Mn_2O_3 : a combined DFT+ U and neutron diffraction study. *Phys. Rev. B* **2013**, 87, No. 184413.
- (115) Barrett, C. A.; Evans, E. Solid solubility and lattice parameter of NiO-MnO . *J. Am. Ceram. Soc.* **1964**, 47, 533.
- (116) Maslen, E. N.; Streltsov, V.; Streltsova, N.; Ishizawa, N. Synchrotron X-ray study of the electron density in α - Fe_2O_3 . *Acta Crystallogr., Sect. B: Struct. Sci.* **1994**, 50, 435–441.
- (117) Fjellvåg, H.; Grønvold, F.; Stølen, S.; Hauback, B. On the crystallographic and magnetic structures of nearly stoichiometric iron monoxide. *J. Solid State Chem.* **1996**, 124, 52–57.
- (118) Redman, M. J.; Steward, E. Cobaltous oxide with the zinc blende/wurtzite-type crystal structure. *Nature* **1962**, 193, 867.
- (119) Kedesdy, H.; Drukalsky, A. X-Ray diffraction studies of the solid state reaction in the NiO-ZnO system. *J. Am. Chem. Soc.* **1954**, 76, 5941–5946.
- (120) Åsbrink, S.; Norrby, L.-J. A refinement of the crystal structure of copper(II) oxide with a discussion of some exceptional esd's. *Acta Crystallogr., Sect. B: Struct. Crystallogr. Cryst. Chem.* **1970**, 26, 8–15.
- (121) Suzuki, T. X-ray study on the binding properties of Cu_2O and Ag_2O crystals. *J. Phys. Soc. Jpn.* **1960**, 15, 2018–2024.
- (122) Ge, S.; Jia, H.; Zhao, H.; Zheng, Z.; Zhang, L. First observation of visible light photocatalytic activity of carbon modified Nb_2O_5 nanostructures. *J. Mater. Chem.* **2010**, 20, 3052–3058.
- (123) Bolzan, A. A.; Fong, C.; Kennedy, B. J.; Howard, C. J. A powder neutron diffraction study of semiconducting and metallic niobium dioxide. *J. Solid State Chem.* **1994**, 113, 9–14.
- (124) Bowman, A. L.; Wallace, T.; Yarnell, J.; Wenzel, R. The crystal structure of niobium monoxide. *Acta Crystallogr.* **1966**, 21, 843.
- (125) Wang, L.; Li, M.-C.; Zhang, G.-H.; Xue, Z.-L. Morphology evolution and quantitative analysis of β - MoO_3 and α - MoO_3 . *High Temp. Mater. Processes* **2020**, 39, 620–626.
- (126) Aleshina, L. A.; Loginova, S. Rietveld analysis of X-ray diffraction pattern from β - Ta_2O_5 oxide. *Crystallogr. Rep.* **2002**, 47, 415–419.
- (127) Schönberg, N.; Overend, W.; Munthe-Kaas, A.; Sørensen, N. A. An x-ray investigation of the tantalum-oxygen system. *Acta Chem. Scand.* **1954**, 8, 240–245.
- (128) Rumble, J. *CRC Handbook of Chemistry and Physics*; CRC Press, 2023.
- (129) Pourbaix, M. *Atlas of Electrochemical Equilibria in Aqueous Solutions*, 2nd ed.; National Association of Corrosion Engineers, 1974.



CAS BIOFINDER DISCOVERY PLATFORM™

STOP DIGGING THROUGH DATA —START MAKING DISCOVERIES

CAS BioFinder helps you find the
right biological insights in seconds

Start your search

CAS
A division of the
American Chemical Society

SI: Roadmap for the development of transition metal oxide cathodes for rechargeable zinc-ion batteries

Caio Miranda Miliante,^{*,†} Storm Gourley,[‡] Brian D. Adams,[¶] Drew Higgins,[‡] and
Oleg Rubel[†]

[†]*Department of Materials Science and Engineering, McMaster University, 1280 Main
Street West, Hamilton, Ontario L8S 4L8, Canada*

[‡]*Department of Chemical Engineering, McMaster University, 1280 Main Street West,
Hamilton, Ontario L8S 4L8, Canada*

[¶]*Salient Energy Inc., Dartmouth, Nova Scotia B3B 1C4, Canada*

E-mail: miliantc@mcmaster.ca

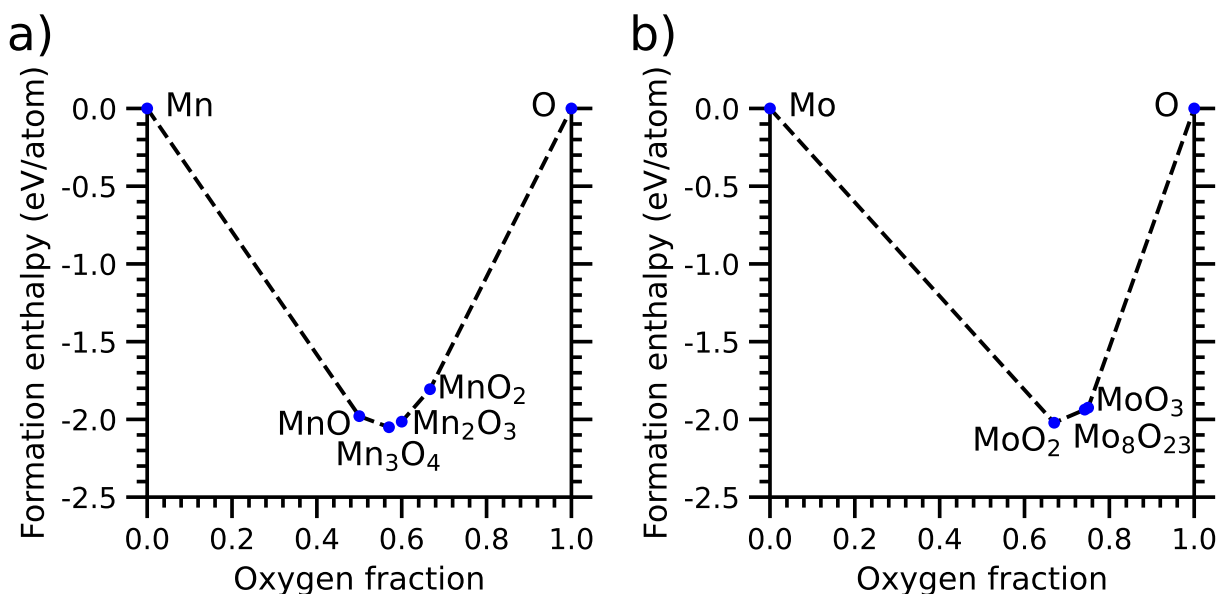


Figure S1: Convex hull diagram for the (a) Mn-O and (b) Mo-O systems depicting the oxides phases that are considered as thermodynamically stable (blue circles). The thermodynamic data for this diagram was obtained from Materials Project.¹

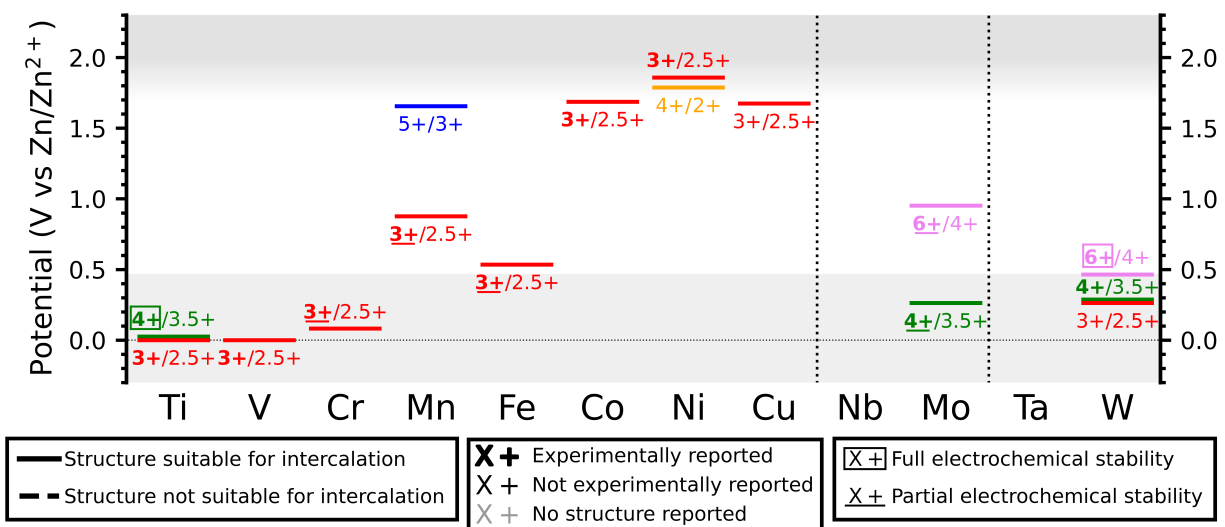


Figure S2: Zinc intercalation potential diagram for transition metal oxide obtained from Density Functional Theory (DFT) calculated thermodynamic data for which half an electron or two electrons are transferred per transition metal. The gray background delimits the calculated potentials for hydrogen evolution reaction (HER) and oxygen evolution reaction (OER) at a pH equal to 5.

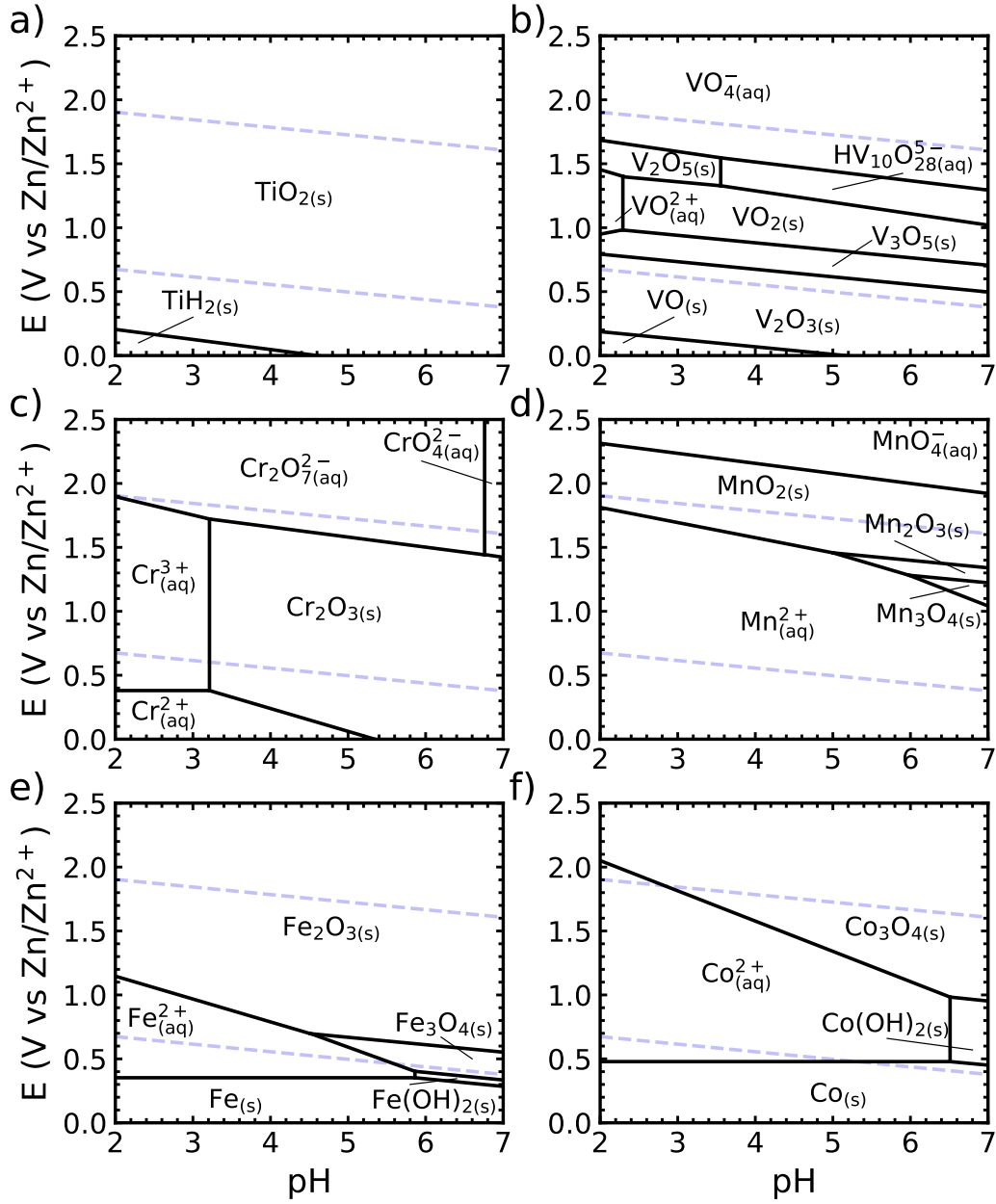


Figure S3: Experimentally obtained Pourbaix diagrams for $M\text{-H}_2\text{O}$ systems where M equals (a) Ti, (b) V, (c) Cr, (d) Mn, (e) Fe, and (f) Co with $[M] = 0.1 \text{ M}$ at 298 K and ambient pressure.² The blue dashed lines represent the theoretical potentials for the hydrogen evolution reaction (HER) and the oxygen evolution reaction (OER).

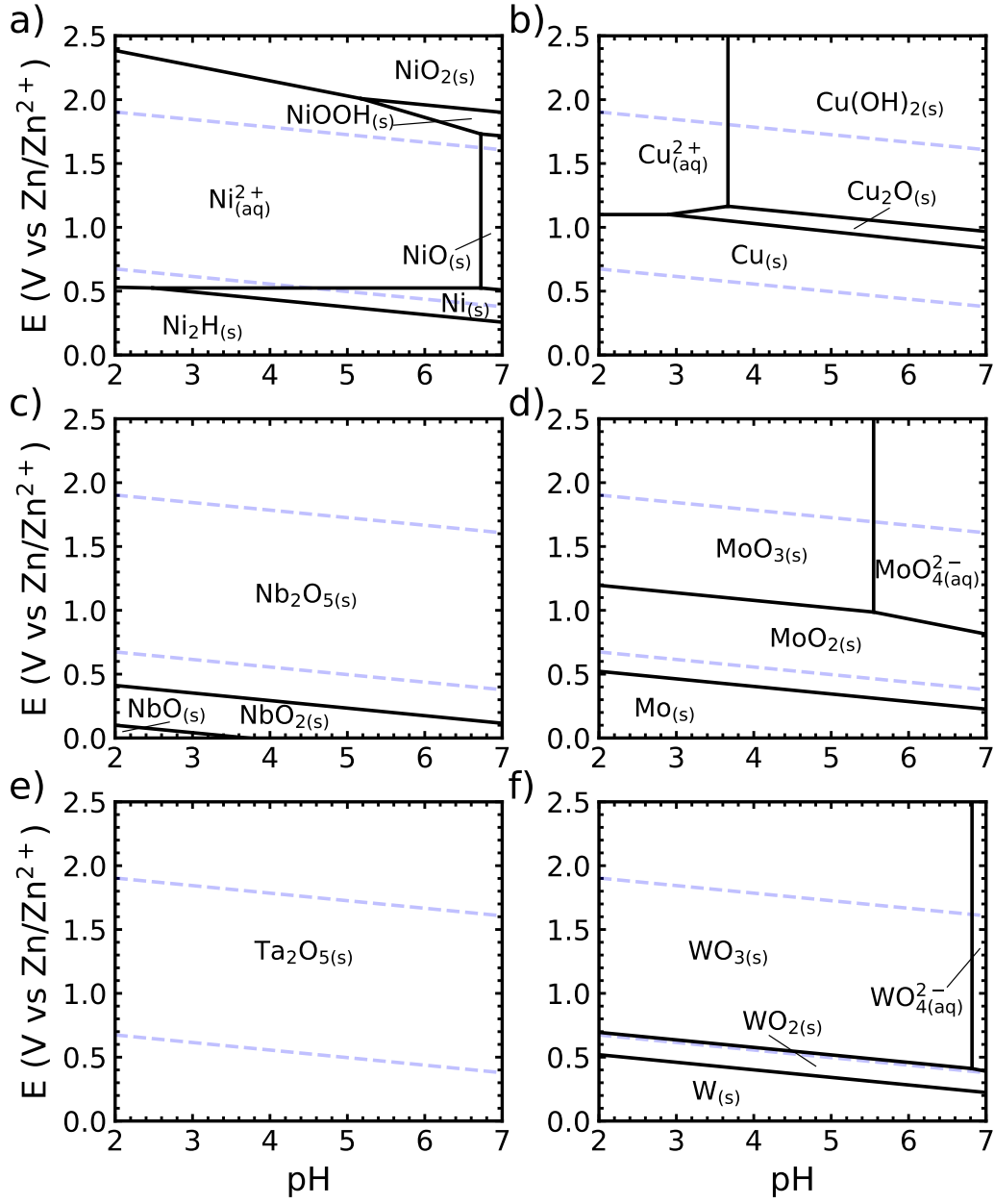


Figure S4: Experimentally obtained Pourbaix diagrams for M -H₂O systems where M equals (a) Ni, (b) Cu, (c) Nb, (d) Mo, (e) Ta, and (f) W with $[M] = 0.1$ M at 298 K and ambient pressure.^{2,3} The blue dashed lines represent the theoretical potentials for the hydrogen evolution reaction (HER) and the oxygen evolution reaction (OER).

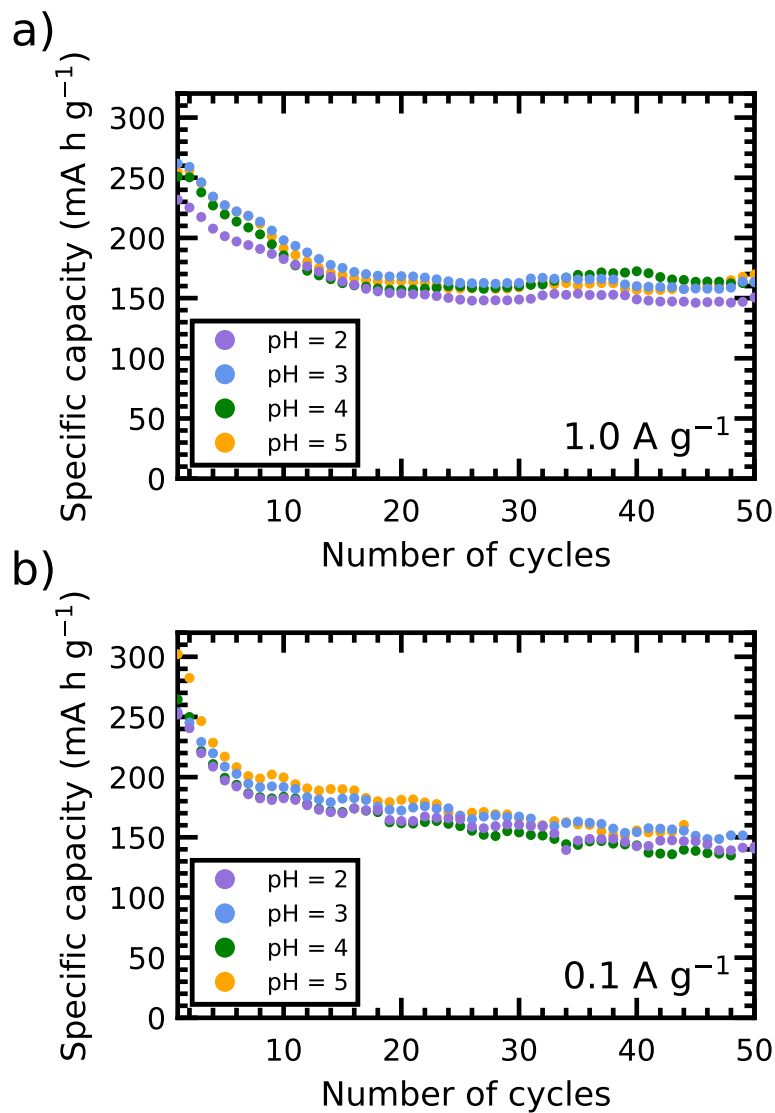


Figure S5: Evolution of $\alpha\text{-MnO}_2/\text{Zn}$ aqueous battery specific capacity through 50 cycles for electrolytes with different pH values at a current density of (a) 1.0 and (b) 0.1 A g^{-1} .

Table S1: Thermodynamic properties of the redox pairs reported by the Battery Explorer tool (solid lines on Figs. 4, 7 and S2).

Element	Pair	Oxide	Materials Project ID	ΔH_f (eV/atom)	$\Delta U_{ins.}$ (eV/atom)	Reference
Ti	4+/3+	TiO ₂	mp-1408285	-3.321	0.181	-
		ZnTi ₂ O ₄	mp-1044664	-2.810	0.192	-
	4+/3.5+	TiO ₂	mp-1400963	-3.441	0.061	-
		ZnTi ₄ O ₈	mp-1392336	-3.099	0.134	-
	3+/2.5+	Ti ₂ O ₃	mp-1046793	-3.174	0.130	-
		ZnTi ₄ O ₆	mp-1046715	-2.759	0.245	-
V	5+/4+	V ₂ O ₅	mp-25233	-2.279	0.011	-
		ZnV ₂ O ₅	mp-1043287	-2.278	0.031	-
	4+/3+	VO ₂	mp-1361684	-2.347	0.134	-
		ZnV ₂ O ₄	mp-1048867	-2.342	0.000	-
		ZnV ₂ O ₄	mp-18879	-	-	4
Cr	3+/2.5+	V ₂ O ₃	mp-1043388	-2.300	0.236	-
		ZnV ₄ O ₆	mp-1043021	-2.137	0.167	-
	5+/4+	Cr ₂ O ₅	mp-1397432	-1.670	0.110	-
		ZnCr ₂ O ₅	mp-1048597	-1.735	0.281	-
		CrO ₂	mp-1400837	-1.857	0.191	-
		ZnCr ₂ O ₄	mp-19410	-2.278	0.000	5
Mn	3+/2.5+	Cr ₂ O ₃	mp-1043379	-2.068	0.300	-
		ZnCr ₄ O ₆	mp-1042605	-1.943	0.224	-
	5+/3+	Mn ₂ O ₅	mp-1104282	-1.152	0.397	-
		Zn ₂ Mn ₂ O ₅	mp-1373342	-1.660	0.281	-
		MnO ₂	mp-25275	-1.774	0.033	6
		ZnMn ₂ O ₄	mp-18751	-1.983	0.000	7
Fe	3+/2.5+	Mn ₂ O ₃	mp-1043363	-1.787	0.227	-
		ZnMn ₄ O ₆	mp-1042996	-1.881	0.110	-
	4+/3+	FeO ₂	mp-1395285	-1.165	0.258	-
		Zn(FeO ₂) ₂	mp-19313	-1.746	0.000	8
Co	3+/2.5+	Fe ₂ O ₃	mp-1378486	-1.433	0.275	-
		Zn(Fe ₂ O ₃) ₂	mp-1043611	-1.527	0.123	-
Ni	4+/3+	CoO ₂	mp-1359404	-0.998	0.083	-
		Zn(CoO ₂) ₂	mp-1040942	-1.407	0.064	-
Ni	4+/3+	NiO ₂	mp-25428	-0.675	0.140	-
		Zn(NiO ₂) ₂	mp-1047462	-1.231	0.000	-
	4+/2+	NiO ₂	mp-25210	-0.685	0.130	-
		ZnNiO ₂	mp-1215685	-1.422	0.083	-
	3+/2.5+	Ni ₂ O ₃	mp-1043875	-0.764	0.214	-
		Zn(Ni ₂ O ₃) ₂	mp-1043670	-1.150	0.077	-

Cu	4+/3+	CuO ₂	mp-504100	-0.520	0.175	-
		Zn(CuO ₂) ₂	mp-1047156	-1.130	0.000	-
	3+/2.5+	Cu ₂ O ₃	mp-1046820	-0.653	0.181	-
		Zn(Cu ₂ O ₃) ₂	mp-1046785	-0.951	0.111	-
Mo	6+/4+	MoO ₃	mp-715584	-1.923	0.003	-
		ZnMoO ₃	mp-1379617	-1.844	0.086	-
	5+/4+	Mo ₂ O ₅	mp-1043432	-1.858	0.111	-
		ZnMo ₂ O ₅	mp-1043221	-1.592	0.373	-
	4+/3+	MoO ₂	mp-1383701	-1.940	0.082	-
		Zn(MoO ₂) ₂	mp-1042597	-1.721	0.091	-
	4+/3.5+	MoO ₂	mp-714883	-1.932	0.106	-
		Zn(MoO ₂) ₄	mp-1044153	-1.696	0.225	-
W	6+/4+	WO ₃	mp-19342	-2.186	0.006	-
		ZnWO ₃	mp-1427680	-1.458	0.481	-
	4+/3.5+	WO ₂	mp-1445593	-1.932	0.106	-
		Zn(WO ₂) ₄	mp-1046548	-1.696	0.225	-
	4+/3+	WO ₂	mp-1380432	-1.724	0.313	-
		Zn(WO ₂) ₂	mp-1041123	-1.508	0.313	-
	3+/2.5+	W ₂ O ₃	mp-1372094	-0.960	0.873	-
		Zn(W ₂ O ₃) ₂	mp-1043075	-0.957	0.758	-

Table S2: Thermodynamic properties of the redox pairs which structural similarities were not observed between the available charged and discharged phase (dashed lines on Fig. 4 and 7)

Element	Pair	Oxide	Materials Project ID	ΔH_f (eV/atom)	$\Delta U_{ins.}$ (eV/atom)	Reference
Ti	5+/4+	Ti ₂ O ₅	-	-3.002	-	-
		ZnTi ₂ O ₅	mp-1404875	-2.906	0.172	-
	3+/2+	Ti ₂ O ₃	mp-458	-3.304	0.000	9
		ZnTi ₂ O ₃	-	-2.753	-	-
	2+/1+	TiO	mp-1203	-2.866	0.043	10
		ZnTi ₂ O ₂	-	-2.329	-	-
V	6+/5+	VO ₃	mp-826024	-1.664	0.339	-
		ZnV ₂ O ₆	mp-540969	-2.198	0.019	11
	3+/2+	V ₂ O ₃	mp-21579	-2.535	0.000	12
		ZnV ₂ O ₃	-	-2.112	-	-
	2+/1+	VO	mp-19184	-2.091	0.022	13
		ZnV ₂ O ₂	-	-1.706	-	-
Cr	7+/6+	Cr ₂ O ₇	-	-1.384	-	-
		ZnCr ₂ O ₇	mp-1341886	-1.587	0.052	-
	6+/5+	CrO ₃	mp-510421	-1.512	0.046	14
		ZnCr ₂ O ₆	mp-1045720	-1.571	0.242	-
	3+/2+	Cr ₂ O ₃	mp-19399	-2.367	0.000	15
		ZnCr ₂ O ₃	-	-1.993	-	-
Mn	7+/6+	Mn ₂ O ₇	mp-28338	-0.881	0.323	16
		ZnMn ₂ O ₇	-	-1.456	-	-
	5+/4+	Mn ₂ O ₅	mp-1104282	-1.152	0.397	-
		ZnMn ₂ O ₅	mp-1043246	-1.536	0.286	-
	3+/2+	Mn ₂ O ₃	mp-1172875	-2.015	0.000	17
		ZnMn ₂ O ₃	-	-1.917	-	-
Fe	5+/4+	Fe ₂ O ₅	mp-1147691	-0.846	0.374	-
		ZnFe ₂ O ₅	mp-1407574	-1.255	0.272	-
	3+/2+	Fe ₂ O ₃	mp-19770	-1.708	0.000	19
		ZnFe ₂ O ₃	-	-1.585	-	-
	2+/1+	FeO	mp-19770	-1.072	0.410	20
		ZnFe ₂ O ₂	-	-1.309	-	-
Co	5+/4+	Co ₂ O ₅	mp-1043418	-0.926	0.000	-
		ZnCo ₂ O ₅	mp-1043279	-1.065	0.222	-
	3+/2+	Co ₂ O ₃	mp-1043418	-0.940	0.296	-
		ZnCo ₂ O ₃	-	-1.454	-	-

	2+/1+	CoO	mp-22408	-1.285	0.000	21
		ZnCo ₂ O ₂	-	-1.230	-	-
Ni	5+/4+	Ni ₂ O ₅	mp-1094139	-0.186	0.513	-
		ZnNi ₂ O ₅	mp-1831183	-0.699	0.378	-
	3+/2+	Ni ₂ O ₃	mp-1043875	-0.764	0.214	-
		ZnNi ₂ O ₃	-	-1.410	-	-
	2+/1+	NiO	mp-19009	-1.219	0.000	22
		ZnNi ₂ O ₂	-	-1.204	-	-
Cu	3+/2+	Cu ₂ O ₃	mp-755040	-0.788	0.046	-
		ZnCu ₂ O ₃	mp-754010	-1.129	0.097	-
	2+/1+	CuO	mp-704645	-0.943	0.000	23
		ZnCu ₂ O ₂	-	-1.104	-	-
	1+/0	Cu ₂ O	mp-361	-0.645	0.000	24
		ZnCu ₂ O	-	-0.895	-	-
Nb	6+/5+	NbO ₃	mp-1179977	-2.460	0.195	-
		ZnNb ₂ O ₆	mp-17177	-2.766	0.000	25
	5+/4+	Nb ₂ O ₅	mp-604	-3.018	0.017	26
		ZnNb ₂ O ₅	-	-2.671	-	-
	4+/3+	NbO ₂	mp-821	-2.895	0.003	27
		ZnNb ₂ O ₄	-	-2.488	-	-
	2+/1+	NbO	mp-2311	-2.288	0.000	28
		ZnNb ₂ O ₂	-	-1.844	-	-
Mo	7+/6+	Mo ₂ O ₇	mp-1180296	-1.373	0.339	-
		ZnMo ₂ O ₇	mp-1042320	-1.861	0.062	-
	6+/5+	MoO ₃	mp-18856	-1.926	0.000	29
		Zn(MoO ₃) ₂	mp-1045736	-1.833	0.122	-
	3+/2+	Mo ₂ O ₃	mp-1371699	-1.491	0.329	-
		ZnMo ₂ O ₃	-	-1.608	-	-
Ta	6+/5+	TaO ₃	mp-1001011	-2.782	0.137	-
		ZnTa ₂ O ₆	mp-17765	-2.995	0.004	25
	5+/4+	Ta ₂ O ₅	mp-554867	-3.018	0.319	30
		ZnTa ₂ O ₅	-	-2.919	-	-
	3+/2+	TaO ₂	mp-20994	-3.037	0.077	31
		ZnTa ₂ O ₄	-	-2.684	-	-
W	7+/6+	W ₂ O ₇	mp-1178760	-1.644	0.304	-
		ZnW ₂ O ₇	mp-1042302	-1.893	0.219	-
	6+/5+	WO ₃	mp-733506	-2.182	0.010	-
		Zn(WO ₃) ₂	mp-1045708	-1.964	0.087	-
	5+/4+	W ₂ O ₅	mp-1043494	-1.865	0.261	-
		ZnW ₂ O ₅	mp-1369997	-1.500	0.476	-

References

- (1) Jain, A.; Ong, S. P.; Hautier, G.; Chen, W.; Richards, W. D.; Dacek, S.; Cholia, S.; Gunter, D.; Skinner, D.; Ceder, G., et al. Commentary: The Materials Project: A materials genome approach to accelerating materials innovation. *APL Mater.* **2013**, *1*, 011002.
- (2) Bale, C. W.; Chartrand, P.; Degterov, S.; Eriksson, G.; Hack, K.; Mahfoud, R. B.; Melançon, J.; Pelton, A.; Petersen, S. FactSage thermochemical software and databases, 2010–2016. *Calphad* **2016**, *54*, 35–53.
- (3) Pourbaix, M. *Atlas of electrochemical equilibria in aqueous solutions*, 2nd ed.; National Association of Corrosion Engineers, 1974; pp 251–255.
- (4) Reehuis, M.; Krimmel, A.; Büttgen, N.; Loidl, A.; Prokofiev, A. Crystallographic and magnetic structure of ZnV_2O_4 : structural phase transition due to spin-driven Jahn-Teller distortions. *Eur. Phys. J. B* **2003**, *35*, 311–316.
- (5) Kemei, M. C.; Barton, P. T.; Moffitt, S. L.; Gaultois, M. W.; Kurzman, J. A.; Seshadri, R.; Suchomel, M. R.; Kim, Y.-I. Crystal structures of spin-Jahn–Teller-ordered MgCr_2O_4 and ZnCr_2O_4 . *J. Phys. Condens. Matter* **2013**, *25*, 326001.
- (6) Fong, C.; Kennedy, B.; Elcombe, M. A powder neutron diffraction study of λ and γ manganese dioxide and of LiMn_2O_4 . *Z. Kristallogr. Cryst. Mater.* **1994**, *209*, 941–945.
- (7) McAndrew, J. Observations on hydrohetaerolite. *Am Min* **1956**, *41*, 268–275.
- (8) Levy, D.; Pavese, A.; Hanfland, M. Phase transition of synthetic zinc ferrite spinel (ZnFe_2O_4) at high pressure, from synchrotron X-ray powder diffraction. *Phys. Chem. Miner.* **2000**, *27*, 638–644.
- (9) Abrahams, S. Magnetic and crystal structure of titanium sesquioxide. *Phys. Rev.* **1963**, *130*, 2230.

- (10) Watanabe, D.; Castles, J.; Jostsons, A.; Malin, A. The ordered structure of TiO. *Acta Crystallogr.* **1967**, *23*, 307–313.
- (11) Andreetti, G.; Calestani, G.; Montenero, A. Refinement of the crystal structure of ZnV_2O_6 . *Z. Kristallogr. Cryst. Mater.* **1984**, *168*, 53–58.
- (12) Nakhal, S.; Hermes, W.; Ressler, T.; Poettgen, R.; Lerch, M. Synthesis, crystal structure and magnetic properties of bixbyite-type vanadium oxide nitrides. *Z. Naturforsch. B* **2009**, *64*, 281–286.
- (13) Dufek, V.; Petrů, F.; Brožek, V. Über sauerstoff-haltige verbindungen vom strukturtyp B1 der ersten vier übergangsmetalle. *Monatsh. Chem.* **1967**, *98*, 2424–2430.
- (14) Stephens, J.; Cruickshank, D. The crystal structure of $(\text{CrO}_3)_\infty$. *Acta Crystallogr. B* **1970**, *26*, 222–226.
- (15) Hill, A. H.; Harrison, A.; Dickinson, C.; Zhou, W.; Kockelmann, W. Crystallographic and magnetic studies of mesoporous eskolaite, Cr_2O_3 . *Microporous Mesoporous Mater.* **2010**, *130*, 280–286.
- (16) Simon, A.; Dronskowski, R.; Krebs, B.; Hettich, B. Die kristallstruktur von Mn_2O_7 . *Angew. Chem.* **1987**, *99*, 160–161.
- (17) Cockayne, E.; Levin, I.; Wu, H.; Llobet, A. Magnetic structure of bixbyite $\alpha\text{-Mn}_2\text{O}_3$: a combined DFT+ U and neutron diffraction study. *Phys. Rev. B* **2013**, *87*, 184413.
- (18) Barrett, C.; Evans, E. Solid solubility and lattice parameter of NiO-MnO. *J. Am. Ceram. Soc.* **1964**, *47*, 533–533.
- (19) Maslen, E.; Streltsov, V.; Streltsova, N.; Ishizawa, N. Synchrotron X-ray study of the electron density in $\alpha\text{-Fe}_2\text{O}_3$. *Acta Crystallogr. B* **1994**, *50*, 435–441.

- (20) Fjellvåg, H.; Grønvold, F.; Stølen, S.; Hauback, B. On the crystallographic and magnetic structures of nearly stoichiometric iron monoxide. *J. Solid State Chem.* **1996**, *124*, 52–57.
- (21) Redman, M.; Steward, E. Cobaltous oxide with the zinc blende/wurtzite-type crystal structure. *Nature* **1962**, *193*, 867–867.
- (22) Kedesdy, H.; Drukalsky, A. X-Ray diffraction studies of the solid state reaction in the NiO-ZnO system. *J. Am. Chem. Soc.* **1954**, *76*, 5941–5946.
- (23) Åsbrink, S.; Norrby, L.-J. A refinement of the crystal structure of copper(II) oxide with a discussion of some exceptional esd's. *Acta Crystallogr. B* **1970**, *26*, 8–15.
- (24) Suzuki, T. X-ray study on the binding properties of Cu₂O and Ag₂O crystals. *J. Phys. Soc. Japan* **1960**, *15*, 2018–2024.
- (25) Waburg, M.; Müller-Buschbaum, H. ZnTa₂O₆, ein neuer Vertreter des tri- α -PbO₂-Typs (mit ergänzenden Daten über ZnNb₂O₆). *Z. Anorg. Allg. Chem.* **1984**, *508*, 55–60.
- (26) Ge, S.; Jia, H.; Zhao, H.; Zheng, Z.; Zhang, L. First observation of visible light photocatalytic activity of carbon modified Nb₂O₅ nanostructures. *J. Mater. Chem.* **2010**, *20*, 3052–3058.
- (27) Bolzan, A. A.; Fong, C.; Kennedy, B. J.; Howard, C. J. A powder neutron diffraction study of semiconducting and metallic niobium dioxide. *J. Solid State Chem.* **1994**, *113*, 9–14.
- (28) Bowman, A.; Wallace, T.; Yarnell, J.; Wenzel, R. The crystal structure of niobium monoxide. *Acta Crystallogr.* **1966**, *21*, 843–843.
- (29) Wang, L.; Li, M.-C.; Zhang, G.-H.; Xue, Z.-L. Morphology evolution and quantitative analysis of β -MoO₃ and α -MoO₃. *High Temp. Mater. Process.* **2020**, *39*, 620–626.

- (30) Aleshina, L.; Loginova, S. Rietveld analysis of X-ray diffraction pattern from β -Ta₂O₅ oxide. *Crystallogr. Rep.* **2002**, *47*, 415–419.
- (31) Schönberg, N.; Overend, W.; Munthe-Kaas, A.; Sørensen, N. A. An x-ray investigation of the tantalum-oxygen system. *Acta Chem. Scand.* **1954**, *8*, 240–245.